

8 Probing Spin, Charge and Orbital Degrees of Freedom by X-Ray Spectroscopy

Eva Benckiser

Max-Planck-Institut für Festkörperforschung

Heisenbergstrasse 1, 70569 Stuttgart

Contents

1	Introduction	2
2	Spin, charge, orbital, and lattice degrees of freedom in epitaxial multilayers	2
3	Soft X-ray spectroscopy	5
3.1	X-ray absorption and dichroism	7
3.2	Resonant X-ray scattering	12
3.3	X-ray resonant reflectometry	13
4	Case studies	16
4.1	Interfacial doping in La_2CuO_4 - LaNiO_3 hybrid structures	17
4.2	Orbital reflectometry of nickelate and vanadate superlattices	19
4.3	Noncollinear magnetic order in nickel oxide heterostructures	24

1 Introduction

The properties of quantum materials, such as $3d$ transition-metal oxides, are largely governed by the collective behavior of their strongly interacting electrons and the material's response is subject to a complex interplay of the local spin, charge, and orbital quantum degrees of freedoms [1]. This manifests itself in various properties such as Mott metal-to-insulator transitions, different types of magnetic order (ferro-, ferri-, and anti-ferromagnetic), orbital order, and unconventional superconductivity [2, 3]. These diverse properties have been extensively studied in bulk materials over the past decades and are of great importance for both, fundamental and applied solid state research.

In recent years, technological advances have enabled the synthesis of heterostructures of quantum material oxides with ultra-thin layers and atomic layer precision, thereby providing different opportunities to manipulate correlated electron systems [4, 5]. Research is primarily aimed at rational materials design through the targeted realization of interfacial reconstructions. The investigation of model systems with specific reconstructions, the generation and understanding of new materials properties, in particular the stabilization of technologically interesting phases under ambient conditions are central motivations of the research area [6–8].

In heterostructures, electronic and magnetic phases that are inaccessible in the bulk can be stabilized and controlled by biaxial strain induced by epitaxy with a single-crystalline substrate, electronic confinement, interfacial doping, or magnetic interactions [9]. The success of these efforts depends on a detailed understanding of the interfacial interactions and reconstructions in these artificially layered materials, which often span only a few atomic layers. The presence of only a very small volume of the material of interest poses a problem for many solid-state spectroscopy methods, such as neutron scattering, muon spin relaxation, or optical spectroscopy, which are normally used to study bulk materials.

In this lecture I like to introduce soft X-ray spectroscopy, with special focus on X-ray absorption and resonant elastic X-ray scattering and reflectivity, as a non-destructive spectroscopic method, which provides important insights into the physics and chemistry of transition-metal oxide heterostructures. As these methods require soft X-rays with variable energy and polarization, it is a synchrotron technique. The rather shallow probing depth of soft X-ray spectroscopy compared to, e.g., neutron scattering, which is sometimes considered a disadvantage in the study of bulk materials, proves to be extremely advantageous for the study of epitaxial heterostructures that are typically not much thicker than 100 nm.

2 Spin, charge, orbital, and lattice degrees of freedom in epitaxial multilayers

A large number of $3d$ transition-metal oxides with strongly-correlated spin, charge, and orbital degrees of freedom crystallize in the perovskite structure with composition ABO_3 , where B is a transition-metal ion, i.e., Sc – Zn, and A either an alkaline-earth (Mg – Ba), or a rare-earth ion (La – Lu) (Fig. 1(a)). This relatively simple, pseudo-cubic structure allows to combine different

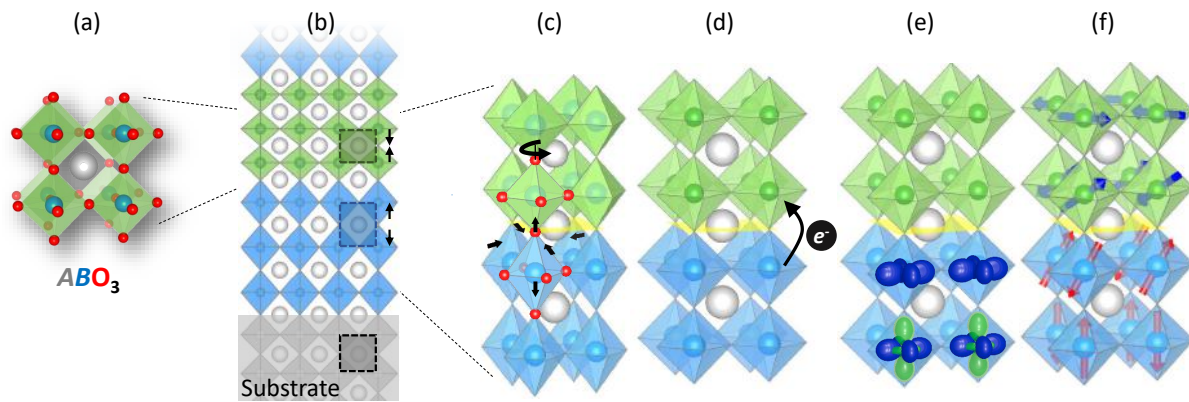


Fig. 1: When combining different transition-metal oxide perovskites, ABO_3 (a), in an epitaxially strained heterostructure (b), different lattice (c), charge (d), orbital (e), and magnetic (f) reconstructions can occur at their interfaces.

compounds in a cube-on-cube fashion in an epitaxial heterostructure (Fig. 1(b)). In this way, an artificially layered material can be created with emergent phases that are not present in the bulk phase diagrams of the individual components.

In fully strained heterostructures, the different B cation positions have a defined in-plane relationship resulting from the adaptation of the lattices at growth temperature. For cube-on-cube growth of the perovskite structure on a cubic substrate, exerting isotropic, biaxial strain (Fig. 1(b)), the simplest modification of the unit cell is a tetragonal distortion. This then leads to elongation (green material) or compression (blue material) of atomic distances along the growth direction, depending on the elastic properties of the material. However, the structural degrees of freedom in transition-metal oxide perovskites allow far more complex distortions, which can be understood in good approximation as tilts and rotations of rigid octahedra around the three cubic axes [10], as indicated in Fig. 1(c). These are determined by the lattice mismatch with the substrate, its crystal symmetry, the choice of the facet, and the connectivity conditions at the interfaces, and thus affect the lengths and angles of the B -O bonds. Therefore, it is important to consider structural distortions in the design, and to study them in detail in the grown heterostructures. *Ab-initio* theories such as density functional theory (DFT) have been shown to provide good predictions for structural modifications (see, e.g., Ref. [11]). Lower-energy scale electronic reconstructions, such as interfacial charge transfer or charge order can occur between multi-valence B ions (Fig. 1(d)). In addition, orbital polarization due to electronic confinement or reduced hopping across the interface due to a change in chemical bonding (Fig. 1(e)), as well as magnetic reconstruction, e.g., due to interfacial exchange coupling, can occur (Fig. 1(f)). The examples in Fig. 1 sketchily show different possible reconstructions, but in section 4 I will give concrete examples for different spin, charge, and orbital reconstruction mechanisms in heterostructures that our group has synthesized and studied in the past years.

The combination of theory, either by considering minimal models that capture the essential properties and *ab-initio* calculations that can investigate small, but relevant material differences, together with different experimental spectroscopy methods has proven to be a very powerful ap-

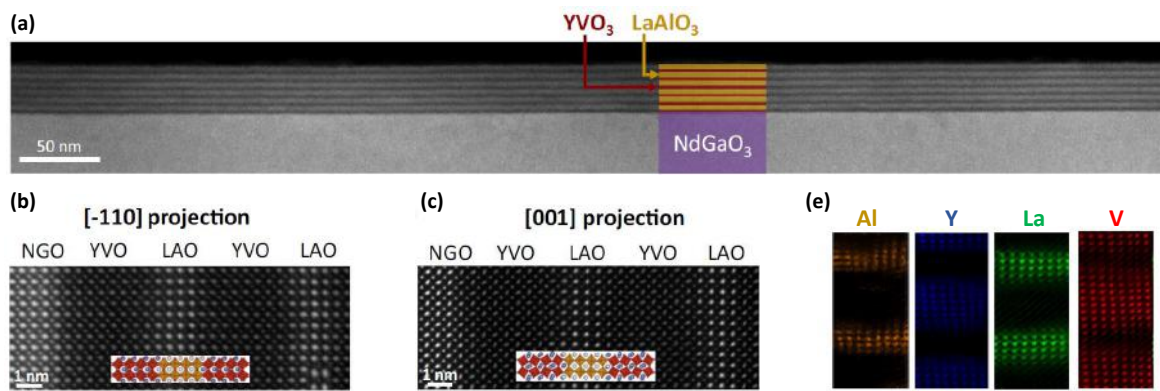


Fig. 2: Scanning transmission electron microscopy (STEM) images of $\text{YVO}_3\text{-LaAlO}_3$ superlattices. (a) Low magnification image, (b,c) High-resolution images for two different crystallographic projections, revealing small structural distortions. (e) STEM-EELS maps show the elemental order in the layers. Reproduced from Refs. [19, 18].

proach to predict and describe the properties of new material combinations. In addition, tremendous progress in the growth of epitaxial complex oxide heterostructures with atomic-layer precision by pulsed-laser deposition [4, 12, 9], magnetron sputtering [13, 14], and molecular-beam epitaxy [15–17] has been made. Nowadays it is possible to grow superlattices with altering layers of only a few unit cells (about 1 nm) of two materials with very high structural and chemical precision. As an example the scanning transmission electron microscopy (STEM) images of a $\text{YVO}_3\text{-LaAlO}_3$ superlattice, grown by pulsed-laser deposition on a NdGaO_3 substrate is shown in Fig. 2. The low-magnification annular dark-field STEM image, shown in Fig. 2(a) covers a lateral range of more than half a μm and the superlattice structure, i.e., the six-times repeated stacking of four unit cells of YVO_3 and eight unit cells of LaAlO_3 , is highly ordered. The images with atomic resolution Fig. 2(b,c), which were taken in different projections with reference to the orthorhombic NdGaO_3 substrate structure, reveal structural distortions in form of tilts and rotations also in the superlattice layers. These structural modifications were reproduced by $\text{DFT}+U$ calculations [18]. Based on the DFT -relaxed structures, the layer-resolved band structures were then calculated and brought into agreement with the orbital occupations determined in the experiment [19] (see section 4). In general, STEM is an important experimental method to study the structural distortions in heterostructures. In addition, electron energy loss spectroscopy (STEM-EELS) allows to study the element specific electronic structure with atomic resolution. However, typically only small spatial volumes are studied (often only a cross-section of $50\text{ nm} \times 50\text{ nm}$ of a sample of 20 nm thickness is analyzed). Furthermore, the preparation of the electron-transparent TEM-lamella and high-energy electron beam damage can be critical issues for oxides, where the oxygen content is variable and often crucial for physical properties such as conductivity and magnetism.

Non-destructive X-ray spectroscopy, which includes X-ray absorption, resonant elastic and inelastic scattering, provides important additional and complementary experimental information, which I will discuss in detail in the following.

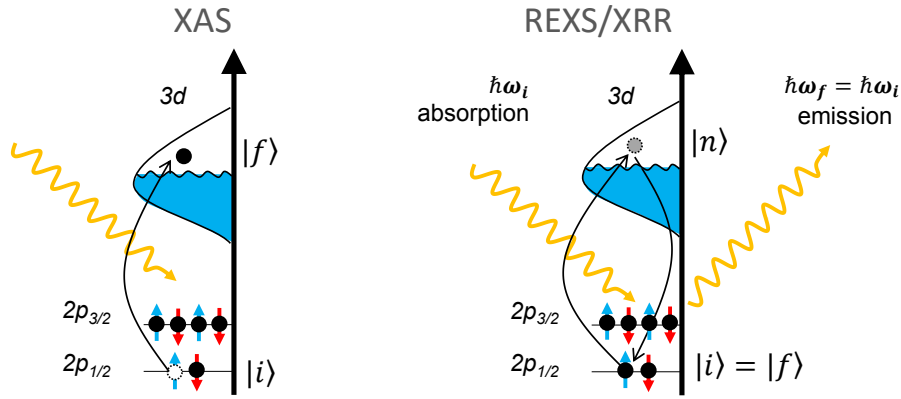


Fig. 3: Schematic of X-ray absorption (XAS; left) and resonant elastic X-ray scattering processes (REXS; right).

3 Soft X-ray spectroscopy

This lecture deals with the study of the spin, charge and orbital degrees of freedom of $3d$ transition-metal oxides. Therefore, we focus on the soft X-ray range as the relevant transition-metal $L_{3,2}$, oxygen K , and the rare-earth $M_{5,4}$ absorption edges fall into this energy window. The latter often occupy the A -cation sites in the ABO_3 perovskites and can lead to interesting exchange interactions between the localized Lanthanoid $4f$ and the transition-metal $3d$ moments (see section 4 and [20]). The soft X-ray range typically covers X-ray energies in the range from 50 to 1500 eV, corresponding to a wavelength range of 413–8.3 Å. We are interested in the spectroscopic information contained in the absorption fine structure that arises from dipole transitions of photo-excited core electrons to empty final states (Fig. 3). Fermi's golden rule provides the transition rate up to second order perturbation theory [21]

$$W = \frac{2\pi}{\hbar} \left| \langle f | H_{int} | i \rangle + \sum_n \frac{\langle f | H_{int} | n \rangle \langle n | H_{int} | i \rangle}{E_i - E_n} \right|^2 \delta(E_i - E_f), \quad (1)$$

where $|n\rangle$ denotes the intermediate (virtual) state and the sum runs over all possible intermediate states with energy E_n . The delta function reflects energy conservation and only depends on the energy of the initial and final state, and not on the energy of the virtual, intermediate states. The interaction Hamiltonian of X-rays with matter can be approximated by [22, 23]

$$H_{int} = \frac{e}{mc} \mathbf{p} \cdot \hat{\mathbf{A}} + \frac{e^2}{2mc^2} \hat{\mathbf{A}} \cdot \hat{\mathbf{A}}, \quad (2)$$

where m denotes the electron mass, \mathbf{p} the electron momentum, and $\hat{\mathbf{A}}$ is the vector potential which characterizes the radiation field

$$\hat{\mathbf{A}}(r_k, t) \propto \sum_{i,k} \frac{1}{\sqrt{k}} \epsilon_i \left(a_{k,i}(t) e^{ikr} + a_{k,i}^\dagger(t) e^{-ikr} \right). \quad (3)$$

The first term in (2) is linear in creation $a_{k,i}$ (emission) and annihilation $a_{k,i}^\dagger$ (absorption) of a photon (with polarization vector ϵ), i.e., it describes processes with changes of ± 1 photons and

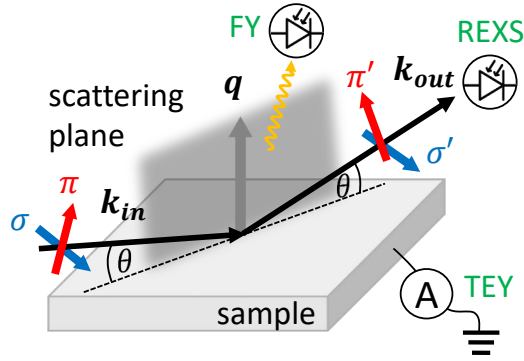


Fig. 4: Schematic of the scattering geometry in a REXS experiment. θ is the scattering angle and k_{in} and k_{out} are the momentum vectors of incident and scattered waves, respectively. The scattering vector is defined by $\mathbf{q} = \mathbf{k}_{in} - \mathbf{k}_{out}$. The components of the polarization vectors are defined parallel π (π') and perpendicular σ (σ') to the scattering plane for the incident (scattered) beam. Absorption can be measured in fluorescence yield (FY) by a photodiode, or in total electron yield (TEY) by the drain current. REXS intensities are detected by a photodiode moving with the 2θ angle.

therefore is relevant for the description of X-ray absorption spectroscopy (XAS). In the second term in (2) the vector potential is applied twice, i.e., it describes processes that change the number of photons by ± 2 , or 0. That is the case in the scattering process (photon-in-photon-out). Resonant X-ray scattering thus is sensitive to the intermediate state (or the final state of the absorption). When the energy is conserved in the scattering process, i.e., $\hbar\omega_{in} = \hbar\omega_{out}$, we refer to it as being elastic and call it resonant elastic X-ray scattering (REXS) or in the case of $\hbar\omega_{in} \neq \hbar\omega_{out}$ to resonant inelastic X-ray scattering (RIXS). In the following we only consider elastic scattering. Restricting our self to electric dipole transitions ($E1$ - $E1$ transitions in Ref. [24]) the interaction Hamiltonian simplifies to $H_{int} \propto \hat{\epsilon}' \mathbf{r} \hat{\epsilon}$, where \mathbf{r} is the dipole operator and $\hat{\epsilon}$ and $\hat{\epsilon}'$ are again the polarization vectors of the incident and scattered light, respectively. They can be expressed by the orthogonal basis vectors perpendicular $\hat{\epsilon}_\sigma$ and parallel $\hat{\epsilon}_\pi$ to the scattering plane, $\hat{\epsilon} = \sigma \hat{\epsilon}_\sigma + \pi \hat{\epsilon}_\pi$, and accordingly for the one of the scattered photon (see sketch in Fig. 4).

In a crystal, each lattice site acts as a scattering center for the incident X-rays and is described by the atomic scattering amplitude

$$F(E, \mathbf{q}) = f_0(\mathbf{q}) + f_{\text{mag}}^{\text{non-res}} + f'(E) + i f''(E). \quad (4)$$

Here $\mathbf{q} = \mathbf{k}_{in} - \mathbf{k}_{out}$ is the scattering vector. The first term in (4), $f_0(\mathbf{q}) \propto Zr_0$, is the so-called Thomson scattering, which is due to elastic scattering by a free charged particle. It arises from the scalar, isotropic polarizability of the scatterer, $f_0(\mathbf{q}) = f(q) \hat{\epsilon}' \cdot \hat{\epsilon}$, where $f(q)$ is the form factor, i.e., the Fourier transform of the particle's charge distribution. The second term is the non-resonant magnetic scattering amplitude $f_{\text{mag}}^{\text{non-res}}$ that contains the interaction between the magnetic field of the incoming wave with the spin of the electrons. As this term is usually small compared to the resonant terms, we will neglect it in the following. The last two terms in (4) are the so-called energy-dependent anomalous dispersion corrections $f'(E)$ and $f''(E)$.

The imaginary part $f''(E)$ is proportional to the XAS cross section, as we will see in the next section, and both terms, $f'(E)$ and $f''(E)$, determine the energy-dependent scattering studied in REXS. In a single-crystal diffraction experiment, photons are scattered with individual atomic scattering amplitudes $F_i(E, \mathbf{q})$ at different lattice sites i at position \mathbf{r}_i in the lattice and interfere. The scattering cross-section then is proportional to $|\sum_i e^{i\mathbf{q}\cdot\mathbf{r}_i} F_i(E, \mathbf{q})|^2$ and in the most general form $F(E, \mathbf{q})$ is a 3×3 tensor with complex entries

$$\hat{F} = \begin{pmatrix} F^{xx} & F^{xy} & F^{xz} \\ F^{yx} & F^{yy} & F^{yz} \\ F^{zx} & F^{zy} & F^{zz} \end{pmatrix}. \quad (5)$$

3.1 X-ray absorption and dichroism

The X-ray mass absorption coefficient $\mu(E)$ is defined by the Lambert-Beer law that describes the transmitted intensity through a material of density ρ and thickness d

$$I = I_0 e^{-\mu(E)\rho d}. \quad (6)$$

The atomic absorption coefficient is energy dependent and in the region between the absorption edges a continuous function, $\mu(E) \propto Z^4/E^3$, where Z is the atomic number. This means that X-rays with higher energy penetrate deeper. The inverse $1/\mu(E)$ is called the attenuation length as it describes the X-ray penetration depth into the material measured along the surface normal, where the intensity of the X-rays falls to $1/e$ of the value at the surface. Soft X-rays are strongly absorbed by matter, and typically the attenuation lengths in materials are less than $0.5 \mu\text{m}$.¹ This means that the experiments have to be carried out in ultra-high vacuum and transmission measurements are not possible for most samples, except for powders or ultra-thin films on transparent membranes such as SiN. However, the decay products of the absorption process can be used to estimate the absorption. There are two principle decay processes of the created core hole: (i) emission of a fluorescence photon, and (ii) Auger decay, followed by secondary processes that emit electrons. The absorption cross section is then proportional to the (total) fluorescence yield (FY) that can be measured by using a photodiode that is placed at a position where elastic scattering is minimal (see Fig. 4). Alternatively, and optimally in addition to FY, the so-called total electron yield (TEY) can be measuring, e.g., by the drain current. When the photoelectrons leave the sample surface, a (small) current is generated by grounding the sample (Fig. 4). Both methods have advantages and disadvantages. Total FY measurements are bulk sensitive, but saturation effects in the vicinity of strong absorption lines can falsify the relative intensities in the fine structure. There are very interesting alternative measurement methods, which are, however, experimentally more complex [25]. The problem of saturation is less relevant in TEY measurements [26], but this type of detection is rather surface sensitive, because it depends on the effective escape depth of the photoelectrons, which is often less than 5 nm, and can vary strongly [27]. Since we focus on thin-film structures, which are usually thinner or about 5 nm thick, surface sensitivity is not a critical issue.

¹The X-ray attenuation length for different solids can be looked up, for example, at <https://henke.lbl.gov>.

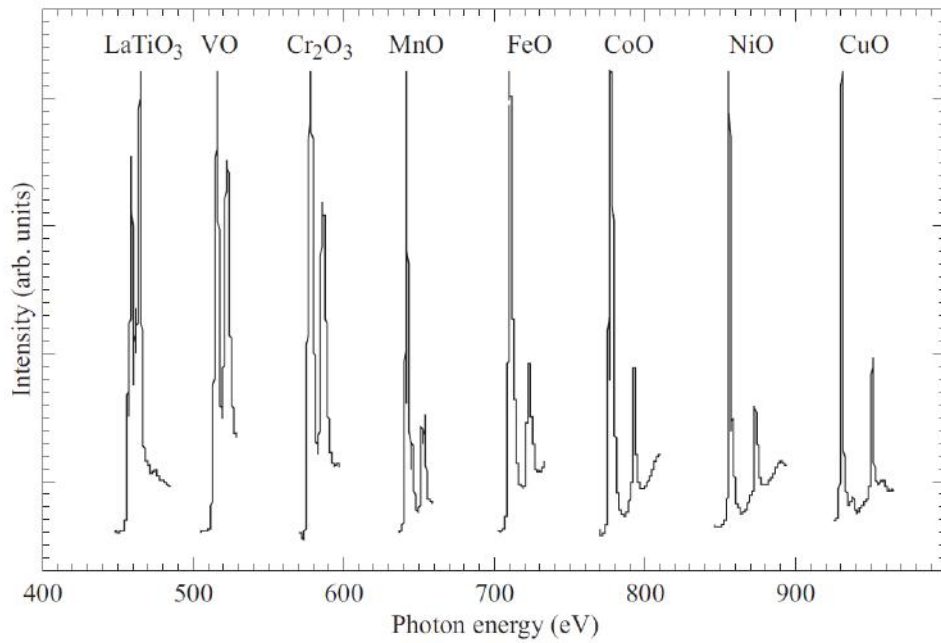


Fig. 5: *L*-edge XAS spectra of a series of 3*d* transition-metal oxides. Taken from Ref. [29]

By varying the energy, which can be done with high resolution (a typical energy band width is ~ 100 meV) and over a wide energy range at a synchrotron beamline, one can observe the above discussed absorption edges, when the energy of the incoming X-rays match the intra-atomic transition energies (see the X-ray data booklet [28]). These transitions have well separated energies, which is the reason for the element sensitivity of the method. As mentioned above, we will focus on electric-dipole transitions, since they have the largest cross section. In forward direction $q \approx 0$, the imaginary part of the scattering amplitude is related to the absorption cross section

$$I_{\text{XAS}} \propto -\frac{1}{E} \text{Im}[\hat{\epsilon} \cdot F(E)] \propto |\langle f | \hat{\epsilon} \cdot \mathbf{r} | i \rangle|^2 \delta(E_i - E_f - \hbar\omega). \quad (7)$$

Only transitions are allowed, which fulfill the dipole selection rules: $\Delta L = 1$, $\Delta m = \pm 1$. It is common to use spectroscopic notation to label specific transitions depending on the involved core level, i.e., the *K*-edge corresponds to $1s$ to, e.g., $2p$ or $4p$, the $L_{3,2}$ to $2p \rightarrow 3d, 4d, \dots$, and the $M_{5,4}$ edge to $3d \rightarrow 4f, 5f$ orbital transitions, where the indices refer to the spin-orbit split core levels $p_{1/2}$, $p_{3/2}$, and $d_{5/2}$, $d_{3/2}$, respectively. For the energy of *K*-edges $E_K \approx Z(Z-1) \times 13.6$ eV provides a good approximation. Here Z is the atomic number of the element and the $Z-1$ term accounts for the screening of the nuclear charge by the second $1s$ electron. The *L*- and *M*-edges have a more pronounced fine structure. Here separated absorption lines are observed due to the spin-orbit splitting of the core levels, e.g., the two $L_{3,2}$ lines arise from the spin-orbit splitting of the $2p_{3/2}$ and $2p_{1/2}$ core levels (see Fig. 3). Their separation accordingly increases in the 3*d* transition-metal row from Sc to Zn as Z increases (Fig. 5). The XAS fine structure measured with higher energy resolution then provides detailed information about the valence state of a particular ion, its spin state, orbital occupation, as well as spin and orbital contribution to the magnetic moment and possible antiferromagnetism. For this purpose,

however, the fine structure must be examined closely, as its interpretation depends on whether the final states are more localized (like f -states) or delocalized (like p -states). The d -states, which are of particular interest to us here, lie somewhere in between, i.e., they are neither fully localized nor fully itinerant [1], which is precisely the cause of the strong correlation of local degrees of freedom that gives rise to their interesting physics.

While K -edge spectra corresponding to transitions from the single $1s$ core level to rather delocalized, empty p states, reflect the site- and symmetry projected unoccupied density of states and are often sufficiently described by mean-field approaches, e.g., local density approximation (LDA) or DFT, the M edges of the rare-earth ions have strong, sharp peaks near the edges that show strong atomic multiplet effects. These multiplet effects show when a core other than a $1s$ is present in the initial state and because of the strong $4f$ localization, since then there is significant overlap of core and valence wave functions in the ground state. This also applies for transition-metal L edges, where the multiplet structure, which is hardly screened in the solid as compared to the core potential, determines the spectral shape and influences the $L_{3,2}$ or $M_{5,4}$ branching ratio [30]. Different valence states show in a shift of spectral weight of the absorption lines. For anions (cations) with different valence state the absorption edge is shifted to lower (higher) photon energies, because of the lower (higher) ionization potential. Information on orbital occupations and magnetic moments can be obtained from the polarization-dependent fine structure. To describe the fine structure of L or M edges, many-body ligand-field cluster calculations have been shown to be particularly successful to determine important parameters, such as the crystal field splittings in NiO and spin states in cobaltates from the comparison with the experimental data [29]. When deriving a minimal tight-binding model from downfolding the DFT band structure to localized Wannier orbitals, important hopping parameters to the ligand ions can be derived in an *ab-initio* fashion from DFT(+ U) [31]. X-ray dichroism, that is the dependence of X-ray absorption on the polarization of the incident photons, occurs when the spherical symmetry at the site of the atom is broken by a magnetic or (crystalline) electric field [35]. Then the charge density around an atom becomes anisotropic. Depending on its origin and the light polarization used to detect it, one distinguishes X-ray natural linear dichroism (charge anisotropy due to crystal field), X-ray magnetic linear dichroism (charge anisotropy parallel and perpendicular to the magnetization axis) [36], and X-ray magnetic circular dichroism [35]. In the first case, for example, the scattering tensor of an atom whose $3d$ states are split by a tetragonal crystal field has unequal diagonal elements along the x and z direction

$$\hat{F} = \begin{pmatrix} F^{xx} & 0 & 0 \\ 0 & F^{xx} & 0 \\ 0 & 0 & F^{zz} \end{pmatrix}. \quad (8)$$

Therefore, the linear polarization dependence of transition-metal L edge XAS provides information on the $3d$ orbital occupation of the system. The intensity of polarized XAS along x , y and z direction is proportional to the number of holes (h) in xz , yz , xy , x^2-y^2 , and $3z^2-r^2$ orbitals that have lobes along that direction. Sum rules allow to relate the d -orbital occupations (h to the total, integrated intensities I_i measured with $i = x, y$ and z linear polarized X-rays

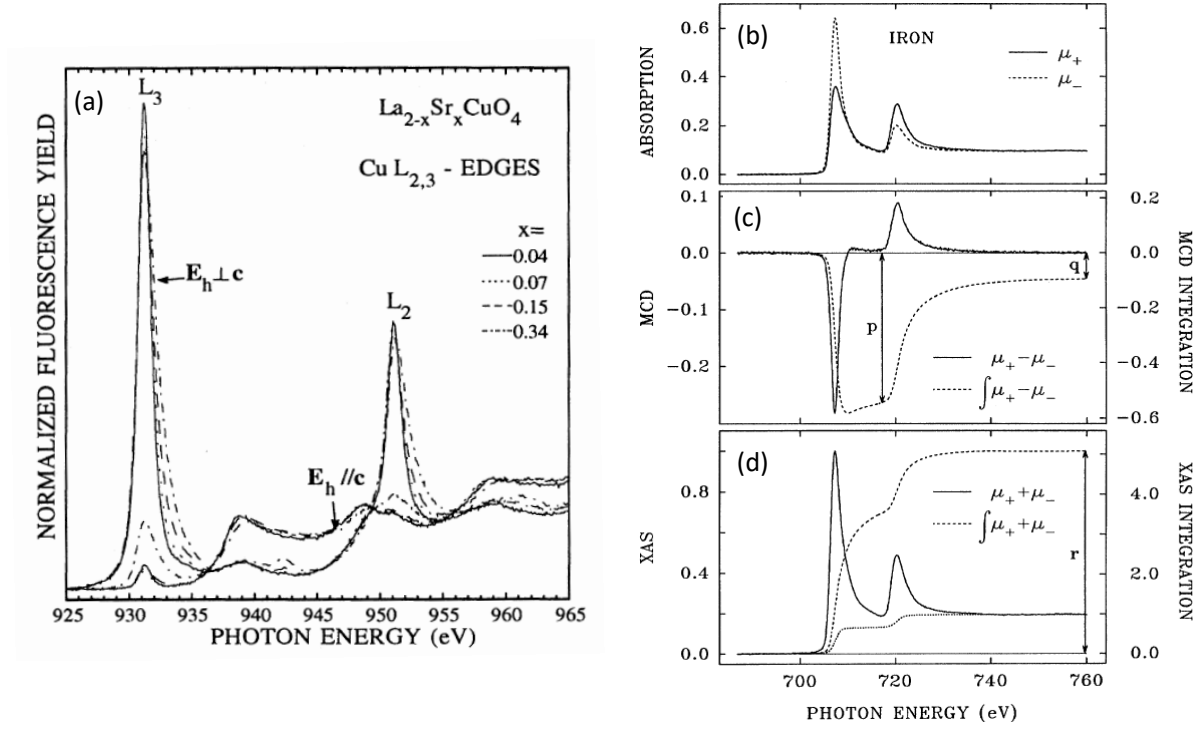


Fig. 6: (a) Example for natural XLD in a $\text{La}_{2-x}\text{Sr}_x\text{CuO}_4$ thin film measured in FY (taken with permission from Ref. [32]), where the data were reproduced from Ref. [33]). (b-d) Example for circular magnetic dichroisms measured in a iron thin film (taken with permission from Ref. [34]).

over the entire $L_{3,2}$ edge [32]

$$\begin{aligned}
 I_x &= \frac{1}{2}h_{xy} + \frac{1}{2}h_{xz} + \frac{2}{3}h_{x^2} \\
 I_y &= \frac{1}{2}h_{xy} + \frac{1}{2}h_{yz} + \frac{2}{3}h_{y^2} \\
 I_z &= \frac{1}{2}h_{xz} + \frac{1}{2}h_{yz} + \frac{2}{3}h_{z^2}.
 \end{aligned} \tag{9}$$

For clarity, we write these for symmetric e_g -orbitals x^2, y^2, z^2 , which are related to the real wave functions as given in Ref. [29]. For $3d$ electron systems with fully filled t_{2g} and partially filled e_g orbitals, the sum rules simplify, and we can directly relate the ratio of e_g holes to the integrated XAS intensities for in-plane ($I_{x,y}$) and out-of-plane (I_z) polarization

$$X = \frac{h_{3z^2-r^2}}{h_{x^2-y^2}} = \frac{3I_z}{4I_{x,y} - I_z}, \tag{10}$$

where $h_{x^2-z^2}$ and $h_{3z^2-r^2}$ denote the number of holes in the $d_{x^2-z^2}$ and $d_{3z^2-r^2}$ orbitals, respectively. Since for t_{2g} -systems the e_g -orbitals have finite hole occupations, the orbital occupations cannot be determined directly from the measured spectra, but cluster calculations can be used, as we will see in section 4.

The Cu- $L_{3,2}$ XAS data measured by Chen *et al.* [33], which are reproduced in Fig. 6(a), provide a very clear example for X-ray natural linear dichroism that originates from differences in

orbital occupation. In the parent compound ($x = 0$) of the high-temperature superconductor $\text{La}_{2-x}\text{Sr}_x\text{CuO}_4$ the valence configuration of Cu is $3d^9$. The Cu ions are square-planar coordinated by four oxygen ions, and the D_{4h} crystal field splitting results in one hole occupying the highest-energy $d_{x^2-y^2}$ orbital in the ground state. The $2p$ core electrons can be excited to this empty state with in-plane x or y polarization ($E \perp c$ in Fig. 6(a)), but no empty states are available for excitation with z polarization ($E \parallel c$ in Fig. 6(a)).

X-ray magnetic circular dichroism (XMCD) is the difference in absorption spectra measured with circular positive (σ^+) and negative (σ^-) polarization, and allows to study magnetism. Again, we consider the $3d$ transition metal L edges, since the magnetic properties are mainly determined by their d -valence electrons. In the absorption process, σ^+ and σ^- polarized photons transfer their angular momentum, $\pm\hbar$, respectively, to the excited photoelectron. Due to spin-orbit coupling in the core level, which is $l+s$ for $2p_{3/2}$ and $l-s$ for $2p_{1/2}$, i.e., opposite in sign, the angular momentum is in part transferred to spin momentum, and the different polarizations create photoelectrons with opposite spins at L_3 and L_2 . The spin-split $3d$ final states can then only be reached by excited photoelectrons with the appropriate spin. The quantization axis is given by the magnetization direction, i.e., the maximum dichroism is measured, when magnetization axis and photon momentum are parallel.

Considering the scattering tensor for cubic, ferromagnetic materials with in-plane aligned magnetization in the scattering plane, the diagonal elements are equal, but two off-diagonal elements are non-zero and proportional to the XMCD signal measured in an absorption experiment [37]

$$\hat{F} = \begin{pmatrix} F^{xx} & iF^{xy} & 0 \\ -iF^{xy} & F^{xx} & 0 \\ 0 & 0 & F^{xx} \end{pmatrix}. \quad (11)$$

Important sum rules can also be derived for circular dichroism. The sum of the integrated intensities I_{L_3} and I_{L_2} of the polarization-averaged spectrum is again proportional to the total number of d -holes (charge sum rule). Following the notation in Ref. [35], we label energy integrals over the XMCD difference spectrum as A for the energy range of the L_3 edge and B for the L_2 edge, respectively. Then the sum rules allows to quantitatively determine the spin moment from the measured intensity $A-2B$, and the orbital moment is obtained from the dichroic intensity $A+B$ [35].

An example for X-ray magnetic circular dichroism in ferromagnetic iron is given in Ref. [34]. The spectra are shown Fig. 6(b), where intensities measured with right and left circular polarized light (labelled with μ^+ and μ^- , respectively) show a clear difference. In the XMCD spectrum (Fig. 6(c)) it can clearly be seen that this difference has an opposite sign for L_3 and L_2 edges. By integrating the spectrum over the respective energy ranges and integrating the polarization-averaged spectrum over the whole energy range (Fig. 6(d)), spin and orbital moments of $m_{\text{spin}} = 1.98$ and $m_{\text{orb}} = 0.085 \mu_B/\text{Fe}$ were determined from the sum rules [34].

3.2 Resonant X-ray scattering

Resonant scattering combines information on spatial modulation from diffraction with the spectroscopic information provided by X-ray absorption in a single experiment [38, 23]. Resonant scattering is element sensitive due to the strong enhancement of the cross section. Furthermore, the strong dependence of the intermediate state on the spin, orbital, and charge configuration of the resonant scattering centers provides access to local properties that I have already discussed in the context of XAS. This information is contained in the energy-dependent $f'(E)$ and $f''(E)$ terms, which are connected via the Kramers-Kronig relation. Both, real and imaginary part are required for the description of resonant elastic X-ray scattering (REXS). If the incident photon energy $\hbar\omega_i$ is very different from the resonance energy $E_i - E_f$ of the system, we say that we are in the non-resonant regime and assume that the scattering is largely independent of energy. Here, however, one must be careful when analyzing scattering intensities as a function of energy, since strong, sharp intensity variation across the resonances in the imaginary part $f''(E)$, (which is proportional to the absorption cross section as discussed above) lead to broader structures in the real part. Depending on how the real and imaginary part mix for a given momentum transfer, anomalous scattering signals can already occur for incident photon energies smaller than those in $f''(E)$. To make this point a little clearer we can look at the example in Fig. 7. Since the fine structure is not captured by tabulated theoretical values [39, 40], the real part is usually obtained via the Kramers-Kronig relation from the imaginary part by including measured or calculated resonance lines. The example shows the procedure for La- $M_{5,4}$. These correspond to transitions from the La $3d$ core electron to completely empty $4f$ states. Therefore, the $f''(E)$ fine structure consists essentially of two sharp Lorentzian lines (middle panel in Fig. 7). When using the Kramers-Kronig relation, sufficient extrapolation of the data outside the measurement range is important, since the integral runs over frequencies from zero to infinity. Therefore, the measured or calculated absorption fine structure data are scaled to tabulated data that are available over a wide energy range (up to 400 keV [40]). From the example in Fig. 7 it can be seen that if we choose an energy well before or in between the resonances in $f''(E)$, intensity variations in f' are still clearly visible, i.e., scattering signals measured even more than 100 eV away from the absorption resonance lines measured in XAS cannot generally be called “non-resonant”. Since the REXS cross section

$$I_{\text{REXS}} \propto \sum_n \left| \frac{\langle f | \hat{\varepsilon} \cdot \mathbf{r} | n \rangle \langle n | \hat{\varepsilon}' \cdot \mathbf{r} | i \rangle}{E_i - E_n} \right|^2 \delta(E_i - E_f - \hbar\omega), \quad (12)$$

is sensitive to the intermediate state $|n\rangle$, which is the final state in XAS, all spectral information that can be gained from XAS, and was discussed above, is contained in the scattered intensity. Moreover, in the REXS experiment, one sees the spatial modulation of the respective properties due to the q dependence. To exploit this, different scan types are used to measure the moment-, energy- and polarization-dependent scattering intensity, which then need to be carefully analyzed, and simulations are often required to obtain quantitative information about modulations of the orbital occupation, charge order, or direction and magnitude of the magnetic moments [23]. However, element-specific electronic and magnetic properties can then be

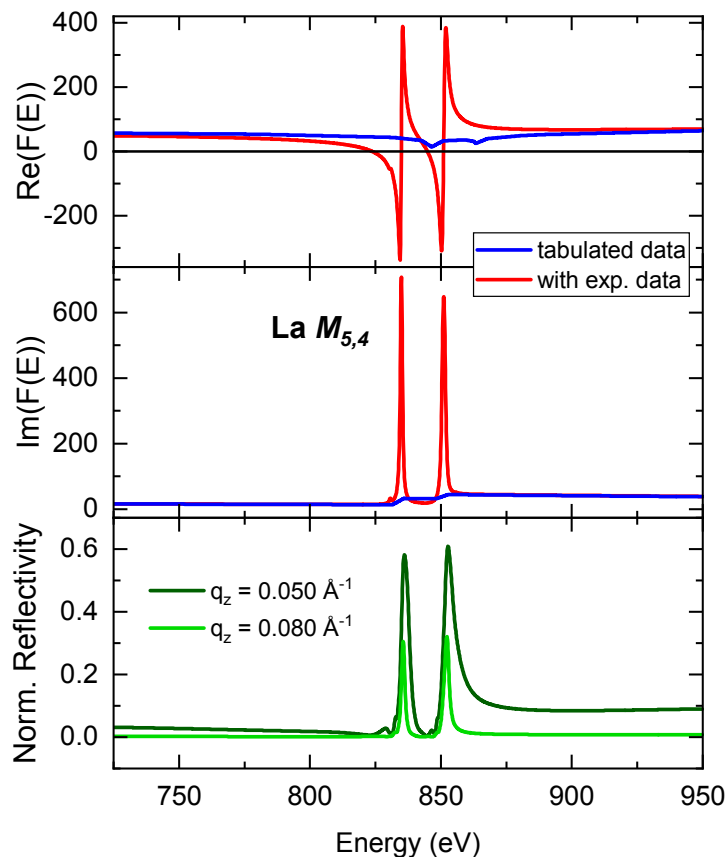


Fig. 7: Real and imaginary part of the energy-dependent scattering factor for the compound LaAlO_3 in the energy range of the $\text{La-M}_{5,4}$ absorption edge. The real $f'(E)$ with resonance (red curve in the top panel) was obtained by Kramers-Kronig transformation of the experimentally determined XAS scaled and extrapolated with the tabulated data of $f''(E)$ (middle panel). The bottom panel shows the normalized X-ray reflectivity of a 30 nm thick film of LaAlO_3 on SrTiO_3 substrate at two different, fixed q_z values over the same energy range.

determined, especially in transition-metal heterostructures, which are not accessible with other experimental techniques, as I will show in the examples in section 4. A disadvantage of REXS in the soft X-ray range is the relatively limited, accessible Ewald sphere, i.e., the limitation of momentum transfer by the wavelength of the incoming X-rays. For soft X-rays, the Ewald sphere is in the order of 0.1 \AA^{-1} , which is sufficient to probe Bragg planes with separation of at least 10 \AA .

3.3 X-ray resonant reflectometry

X-ray reflectometry, usually measured in the hard X-ray range far away from strong resonances, is an established method for the structural characterization of thin films and multilayers (see sketch in Fig. 8). It is based on the simple concept of multiple reflection and refraction of radiation at a surface and interfaces. In a typical experiment, the intensity of a scattered beam $R(\theta)$, normalized to the incoming intensity I_0 , is measured as a function of the incident angle θ .

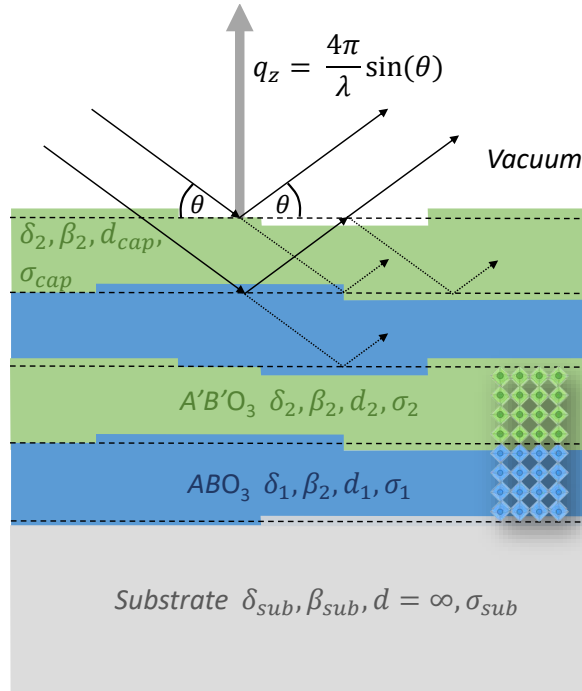


Fig. 8: *Specular scattering geometry ($\theta_{in} = \theta_{out}$, q_z parallel to the surface normal) and typical set of structural parameters used to simulated XRR data. The sketch shows an example of an ABO_3 - $A'B'O_3$ superlattice with two repetitions of the bilayer, and with energy-dependent optical constants $\delta_{1,2}(E)$ and $\beta_{1,2}(E)$. The layer thicknesses d and root-mean-square roughnesses σ of different layers are usually fitting parameters.*

In such a scattering process, a momentum $q = 4\pi \sin(\theta)/\lambda$ is transferred.² The term reflectometry refers to specular scattering with $\theta_{in} = \theta_{out}$, i.e., q_z points along the surface normal z (Fig. 8). As is known from optics, when light emerges from an optically denser medium into an optically thinner one, there is a critical angle θ_c (depending on the wavelength λ), below which all incoming intensity is reflected on the surface (total internal reflection). Above θ_c , part of the radiation penetrates the material, interacts and parallel beams obtain a phase difference and interfere [41]. This results in characteristic features in the X-ray reflectivity of multilayers, such as Kiessig fringes, superlattice peaks, and changes in slope due to surface and interface roughness. By fitting the structures using calculated scattering factors (see Refs. [40, 39]) structural parameters, such as the individual layer thicknesses and roughnesses (d_i and σ_i in Fig. 8), can be determined with high precision. When analyzing X-ray resonant reflectivity (XRR) data measured at energies near or at the resonances, and where one aims to determine layer-resolved changes in the energy-dependent scattering factors, the structural parameters are kept fixed. Since only an out-of-plane momentum transfer is considered, the layers can be treated as a homogeneous medium and the reflectivity can be described in the so-called optical approach. To do this, we introduce the complex refractive index in the X-ray range³

²It is practical to note the conversion between wavelength λ and energy E : $\lambda[\text{\AA}] = 12398.4244/E[\text{eV}]$

³In some references the refractive index is defined by $n = 1 - \delta - i\beta$, consistent with an opposite sign in the wave equation.

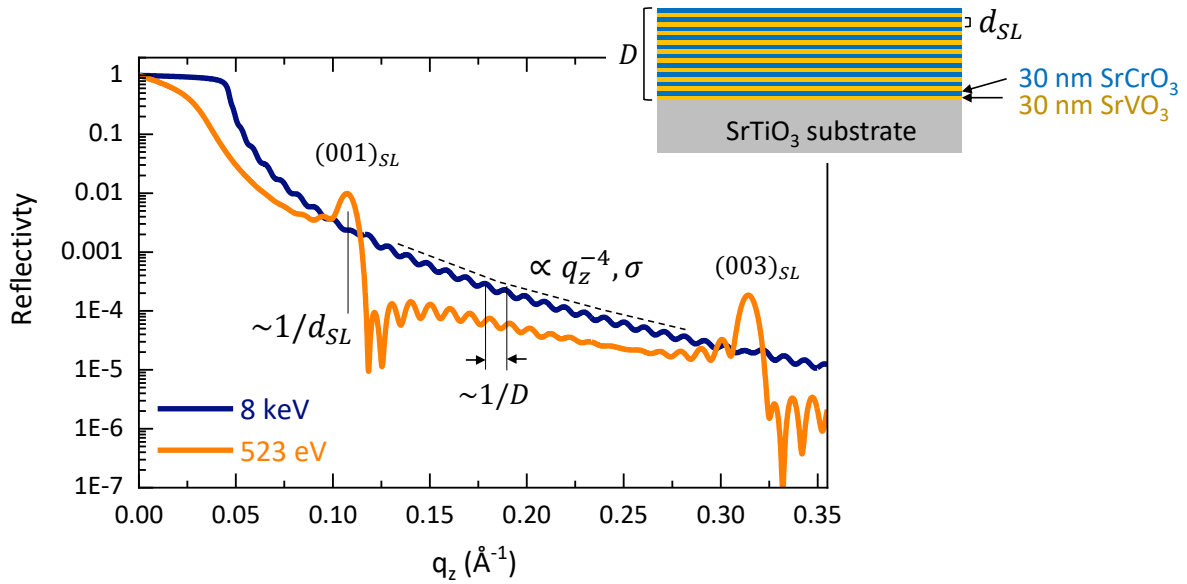


Fig. 9: Example for the momentum-dependent XRR from a superlattice composed of ten repetitions of a $[\text{SrVO}_3$ (30 nm) / SrCrO_3 (30 nm)] bilayer on a SrTiO_3 substrate. The labels indicate characteristic features in the reflectivity curve, such as the total thickness D , the bilayer thickness d_{SL} , and possible surface roughness σ . The simulated XRR curves are shown for X-ray energies at 8 keV, i.e., far from resonances, and close to the V - L_2 -resonance at 523 eV to demonstrate the effect of the energy-dependent change of contrast from the scattering factors. Since both materials have very similar electron densities the superlattice reflections $(00l)_{SL}$ are invisible in the non-resonant data, but clearly show in the V - L_2 data (see Fig. 12(a)). Note that the $(002)_{SL}$ reflection is not allowed in this specific superlattice structure with identical thicknesses of SrCrO_3 and SrVO_3 and no interface roughness.

$$n = 1 - \delta + i\beta. \quad (13)$$

At energies (E) close to the resonance edges in a material, the atomic scattering factor (Eq. 4) shows strong variations in the energy-dependent real $f'(E)$ and imaginary $f''(E)$ part of the dispersion corrections. In case of forward scattering ($\mathbf{Q} \approx 0$) and negligible non-resonant magnetic scattering $f_{\text{non-res}}^{\text{mag}}$ [42], equation (4) reduces to

$$F(\mathbf{q} \approx 0, E) = Z^* + f'(E) + if''(E), \quad (14)$$

where $Z^* = Z - (Z/82.5)^{2.37}$ is the atomic number Z with a small relativistic correction [28]. The optical theorem connects the imaginary part of the scattering factor to the dielectric function $\varepsilon(E)$ by

$$f''(E) = -\frac{E^2}{2\pi(c\hbar)^2 N_p} \text{Im} \sqrt{\varepsilon(E)}, \quad (15)$$

where c is the speed of light, \hbar the Planck constant, N_p the number of photons, and E the energy of the X-rays. Just like the $F(E)$ (Eq. 5), $\varepsilon(E)$ has the form of a 3×3 tensor

$$\hat{\varepsilon} = \begin{pmatrix} \varepsilon^{xx} & \varepsilon^{xy} & \varepsilon^{xz} \\ \varepsilon^{yx} & \varepsilon^{yy} & \varepsilon^{yz} \\ \varepsilon^{zx} & \varepsilon^{zy} & \varepsilon^{zz} \end{pmatrix}, \quad (16)$$

with complex entries $\varepsilon^{ij} = (\varepsilon_1)^{ij} + i(\varepsilon_2)^{ij}$ ($i, j = x, y, z$) that are related to δ^{ij} and β^{ij} by $\varepsilon_1^{ij} = (1 - \delta^{ij})^2 - (\beta^{ij})^2$ and $\varepsilon_2^{ij} = 2(1 - \delta^{ij})\beta^{ij}$. In a compound consisting of N different atoms, δ and β are then given by the sums of atomic scattering factors weighted by the density ρ of the material

$$\delta(E) = \frac{2\pi\rho r_0(c\hbar)^2}{ME^2} \sum_{j=1}^N C_j (Z_j^* + f_j'(E)) \quad (17)$$

$$\beta(E) = \frac{2\pi\rho r_0(c\hbar)^2}{ME^2} \sum_{j=1}^N C_j f_j''(E). \quad (18)$$

Here C denotes the number of atoms of type j per formula unit, M is the molar weight of the compound, and r_0 is the Thompson scattering amplitude (classical electron radius). Furthermore, we know from equation (7) that $f''(E)$ is proportional to the X-ray absorption cross section I_{XAS} . Therefore, we can combine both relations to obtain reliable resonant tensor entries δ and β , for the different layer stacks, as shown in Fig. 7 for LaAlO_3 . These can then be further modeled to obtain layer-specific optical constants, corresponding to the different reconstruction scenarios in a given material system. These can be, for example, different, layer-dependent orbital polarizations, as we have studied in the examples I will show in the next section 4.

Depending on the symmetry of the material, the dielectric tensor (Eq. 16), just like the scattering tensor takes on a simplified form [43]. For example, for materials with cubic, tetragonal and orthorhombic symmetries, all non-diagonal elements are zero. Going from orthorhombic to tetragonal and cubic symmetry, the tensor further simplifies with $\varepsilon_{xx} = \varepsilon_{yy}$ for tetragonal and $\varepsilon_{xx} = \varepsilon_{yy} = \varepsilon_{zz}$ for cubic symmetries. Just as for $F(E)$, the dielectric tensor of ferromagnetic materials has specific, non-zero off-diagonal elements that are proportional to the X-ray magnetic circular dichroism (XMCD). Therefore, X-ray resonant magnetic reflectivity allows to measure magnetic moments of deeply buried atomic, magnetic layers in a multilayer [44].

4 Case studies

In the following, I will present some of our studies on complex oxide heterostructures, each with a different type of interface reconstruction as outlined in the introductory Fig. 1, and which we investigated using the different X-ray spectroscopy techniques presented in the previous section. In the first example, we show how the element sensitivity of XAS can be used to investigate an interfacial doping mechanism in a cuprate-nickelate hybrid structure. The second example shows how linearly polarized resonant X-ray reflectometry can be used to determine depth-resolved orbital polarization profiles in a quantitative manner. The last example shows how resonant elastic X-ray scattering provides unique information about noncollinear magnetic orderings and how such ordered moments can interact with other moments across interfaces.

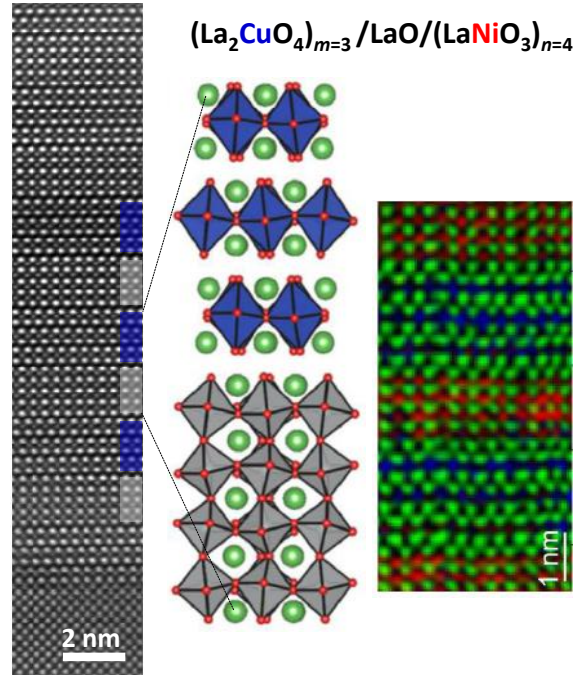


Fig. 10: *Left panel: High-angle annular dark field (HAADF) STEM image of the $m = 3$, $n = 4$ cuprate-nickelate hybrid structure grown on $(\text{LaAlO}_3)_{0.3}(\text{Sr}_2\text{AlTaO}_6)_{0.7}$ (LSAT) substrate. Middle panel: Sketch of the bilayer structure with the composition indicated in the above label. Right panel: Spatially-resolved elemental distribution extracted from the electron energy loss spectra (EELS) with color code: La–green, Cu–blue, and Ni–red, respectively. Reproduced with permission from Ref. [45].*

4.1 Interfacial doping in La_2CuO_4 - LaNiO_3 hybrid structures

Layer-by-layer oxide molecular-beam epitaxy allows to grow complex oxides with atomic layer precision. We used this technique to synthesize a cuprate-nickelate multilayer structure (Fig. 10) and showed that these structures allow a clean separation of dopant and doped layers. The multilayer growth of La_2CuO_4 and LaNiO_3 can only be achieved with two LaO layers separating cuprate and nickelate blocks. This translates to an extra $\text{La}^{3+}\text{O}^{2-}$ atomic layer in the bilayer formula $(\text{La}_2\text{CuO}_4)_m/\text{LaO}/(\text{LaNiO}_3)_n$ (m, n integers), resulting in an additional charge of +1 at each interface, which we suspected to lead to a change in the nickel or copper electronic structure. We investigated this in detail using XAS and explicitly exploited element sensitivity. The spectra measured with soft X-rays across the Cu- $L_{3,2}$ and Ni- $L_{3,2}$ absorption edges are shown in Fig. 11(a,b). The measurements were performed with linearly polarized X-rays parallel (I_x) and perpendicular (I_z) to the interfaces. While the Cu- L spectra are characteristic of Cu^{2+} [46], the Ni- L edge spectrum shows signs of a mixture of Ni^{2+} and Ni^{3+} . The octahedral crystal field splits the Cu and Ni $3d$ levels into energetically lower t_{2g} and higher e_g orbitals. An additional elongation of the CuO_6 and NiO_6 octahedra along the $[001]$ direction, observed by STEM [45], leads to a further splitting of the e_g orbitals. This is reflected in the polarization dependence, where I_x (I_z) probes holes in the $d_{x^2-y^2}$ ($d_{3z^2-r^2}$) orbital. The resulting normalized linear dichroic difference spectrum $(I_x - I_z)/(2I_x + I_z)$ at the Cu- L edge is very

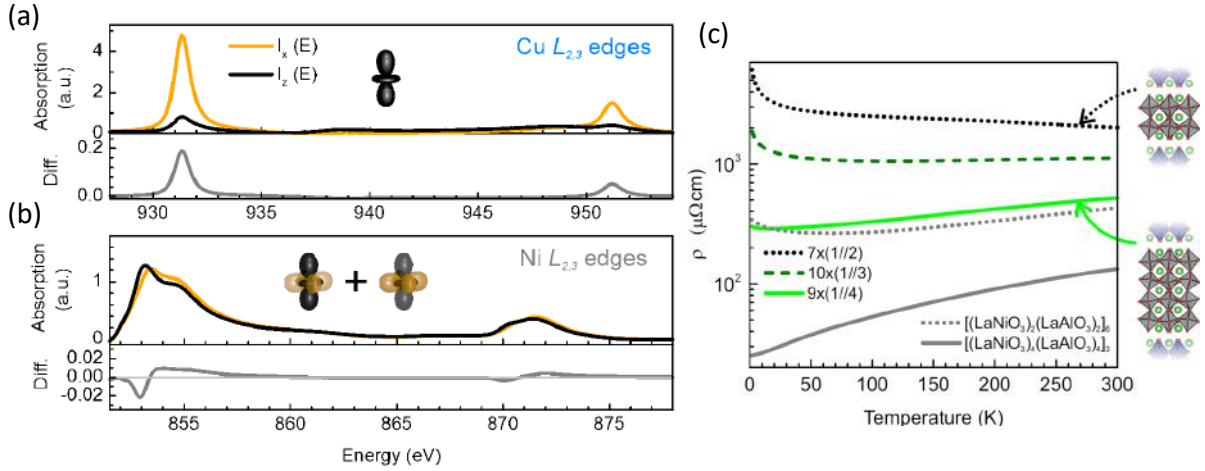


Fig. 11: XAS spectra measured with the polarized X-rays parallel (orange curves) and perpendicular (black curves) to the sample surface across (a) the Cu- $L_{3,2}$ (b) the Ni- $L_{3,2}$ edges for the $m=3$, $n=4$ cuprate-nickelate hybrid structure shown in Fig. 10. In the bottom panels the normalized dichroic signals (grey curves) are shown. (c) Temperature-dependent resistivity of $[(\text{La}_2\text{CuO}_4)_m/\text{LaO}/(\text{LaNiO}_3)_n]_l$ ($m=1$, $n=2, 3, 4$, and $l=7, 10, 9$) with average formal Ni valences of 2.5+, 2.67+, and 2.75+ for $n=2, 3, 4$, respectively, compared to $[(\text{LaNiO}_3)_n(\text{LaAlO}_3)_k]_k$ superlattices with $n=2, 4$ and $k=6, 3$ with 3.0+ Ni valence. Taken with permission from Ref. [45].

pronounced (Fig. 11(a) to be compared with Fig. 6(a)) and arises from a Jahn-Teller distortion that lowers the energy of the $d_{3z^2-r^2}$ orbital [32], leaving a hole in the $d_{x^2-y^2}$ orbital for the XAS final state. The Ni- L edge spectra also show linear dichroism, although less pronounced. To quantify this effect, we used the sum rules for e_g linear dichroism (Eq. 10). While DFT+ U results show $X = 1$ for bulk LaNiO_3 with rhombohedral structure (space group $R\bar{3}c$, where all Ni-O distances are equal), we find a smaller $X_{\text{av}} = 0.94$ from XAS, corresponding to a higher $d_{3z^2-r^2}$ occupation on average in the LaNiO_3 stacks in the hybrid structures [45]. The layer-resolved DFT+ U calculations show that the effect is most pronounced in the interface layers ($X_{IF} = 0.84$), which correlates with the stronger elongation of the interfacial NiO_6 octahedra in the $[001]$ direction as seen by STEM [45]. The corresponding value in the central layers is $X_C = 0.91$.

In addition, DFT+ U predicts a charge disproportionation between neighboring in-plane Ni sites that occurs predominantly in the interface layers and causes a band gap in the density of states of the interface layers. To test this prediction we performed in-plane electronic transport measurements on different hybrid structures with $m=1$ and decreasing LaNiO_3 layer thickness $n=4, 3, 2$ (Fig. 11 (c)). The temperature-dependent resistivity shows metallic behavior for $n=4$, which we attribute to currents running through the inner, at most weakly disproportionated, metallic LaNiO_3 layers. When decreasing LaNiO_3 from four to three monolayers, we observe a metal-to-semiconductor transition, and finally, for $n=2$, a semiconducting behavior. Consistent with this observation, DFT+ U results for $n=2$ indicate a band gap of 0.28 eV [45]. To distinguish confinement and doping effects, we compare the $(\text{La}_2\text{CuO}_4)_m/\text{LaO}/(\text{LaNiO}_3)_n$ hybrid

structures with $[(\text{LaNiO}_3)_n(\text{LaAlO}_3)_k]_k$ ($n=2, 4$ and $k=6, 3$) superlattices, where the nickelate layers are confined to the same thickness, while remaining undoped (Ni^{3+}). The latter superlattices will be discussed in detail in the next section. Leaving differences in the lattice parameters of the two systems aside, it is interesting to note that the resistivity of the LaNiO_3 - LaAlO_3 superlattice with two nickelate layers is comparable to the nickelate-cuprate hybrid structure with four nickelate layers. This implies that only the inner two layers are conducting, as predicted by the DFT calculations. In conclusion, our study on the cuprate-nickelate hybrid structures showed that doped electrons are accommodated primarily in the interfacial nickelate layers, where they induce a digital modulation of the Ni valence state and a rearrangement of the Ni-3d orbital occupation.

4.2 Orbital reflectometry of nickelate and vanadate superlattices

The d orbital occupations and the strength of hybridization with the oxygen ligands determine the electronic transport properties and the magnetic exchange interactions and their anisotropy, via the Goodenough-Kanamori-Anderson (GKA) rules for superexchange [47, 48]. As pointed out in the introductory section a common effect created at interfaces is the confinement of electrons. We have studied heterostructures of two prototypical correlated oxides, Mott-Hubbard insulating YVO_3 and the negative charge-transfer system $R\text{NiO}_3$ ($R = \text{rare-earth ion}$) [49]. While the vanadates are a $3d-t_{2g}$ electron system, in the nickelate the higher-lying e_g states are partially occupied. If we consider an interface of LaNiO_3 (YVO_3) with a wide band-gap insulator, such as LaAlO_3 , the (virtual) hopping of electrons along the Ni(V)-O-Al bond is largely suppressed, due to the band-gap of LaAlO_3 , which leads to the preferential occupation of the orbitals with lobes in the plane of the interface. In addition, the character of the Ni-O-Al or V-O-Al chemical bond changes, which is accompanied by a change in the oxygen hybridization of the d states. Last but not least, the modification of the local crystal fields impacts orbital polarization, as at the interface it is expected to be different from both, the bulk as well as in layers deeper in the stack that are further away from the interfaces. In superlattices of LaNiO_3 or YVO_3 with LaAlO_3 , this interface is repeated several times periodically (see Fig. 2), which facilitates the investigation by means of XRR. The modulation in the electronic structure of interface and central layer in stacks of LaNiO_3 or YVO_3 is seen in so-called orbital reflectometry, where one measures the XRR with linear polarized light. A simple calculation of the structural factors shows this sensitivity (Fig. 12). If we consider a symmetric superlattice with the same thickness of stacks of two compounds ABO_3 and $AB'O_3$ (the example in Fig. 12(a) show a (6/6) superlattice, with six pseudo-cubic unit cell of each material), without any symmetry breaking the even-order, $(00l)$, $l=2, 4, \dots$ superlattice peak intensities vanish. If, however the electronic structure of interface (IF) and central (C) layers are different, resulting in different scattering factors f^{IF} and f^C due to interface reconstructions, this selection rule is broken and the intensity becomes proportional to the difference in the scattering factors (Fig. 12(b)). The same sensitivity for interface reconstructions arises in asymmetric (8/4) and (4/8) at the (003) reflection (Fig 12(c)). We take advantage of this in orbital reflectometry and simulate the polarization-

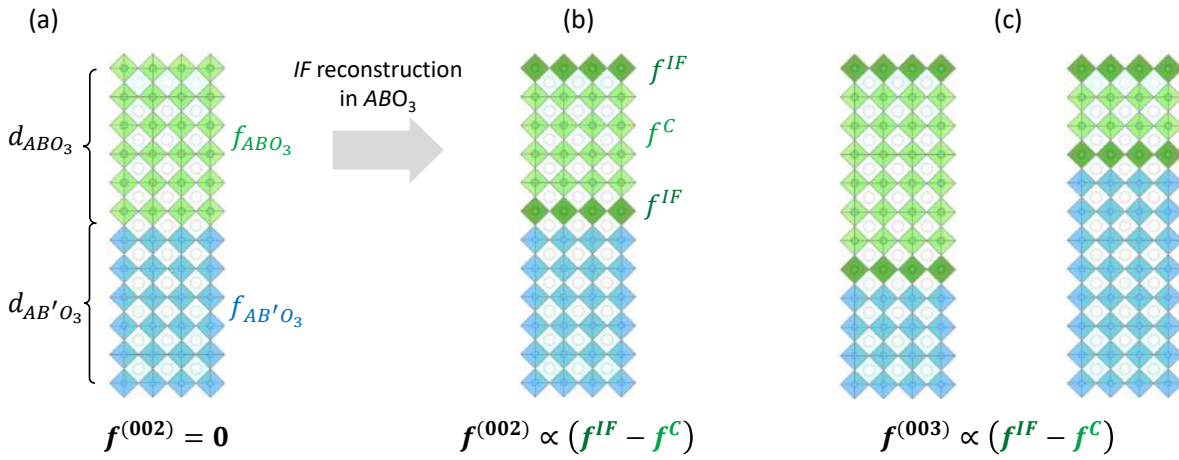


Fig. 12: Scattering factors for different stacking of two materials ABO_3 (green) and $AB'O_3$ (blue) in a superlattice (the shown bilayer is repeated several times). (a) In case of a symmetric SL ($d_{ABO_3} = d_{AB'O_3}$) the (002) reflection of the SL structure vanishes. (b) When the ABO_3 interface layers reconstruct, resulting in different scattering factors in interface (f^{IF}) and central layers (f^C), the (002) reflection becomes allowed. (c) In the case of an asymmetric stacking sequence with ($2d_{ABO_3} = d_{AB'O_3}$ (left) or $d_{ABO_3} = 2d_{AB'O_3}$ (right)), the (003) superlattice reflection is most sensitive to a difference of f^{IF} and f^C .

dependent spectra, measured at fixed momentum transfer at (002) or (003) as a function of energy over the corresponding L edges of Ni or V. To ensure a unique fitting result, we only allow a redistribution of the dichroism in f^{IF} and f^C , so that the layer-weighted average, measured in XAS is fixed, i.e., $I_{XAS} \propto n \text{Im}(f^{IF}) + m \text{Im}(f^C)$ with n, m the number of unit cells of IF and C layers, respectively. The results of the simulations that best match the experimentally measured XRR then provide layer-specific linear dichroism spectra that can be quantitatively evaluated using the sum rules or cluster calculations to obtain orbital occupancies.

Since the t_{2g} orbital lobes point between the B -O bonds, while for e_g orbitals they point along the bonds, it is interesting to systematically compare reconstructions at YVO_3 - $LaAlO_3$ and $RNiO_3$ - $LaAlO_3$ interfaces. as I will discuss in the following. Our studies on $LaNiO_3/LaAlO_3$ superlattices showed that both, epitaxial strain and confinement effects at the interface lead to changes in the Ni- e_g orbital polarization depth profiles [50, 51]. In YVO_3 - $LaAlO_3$ superlattices the interface effects produce an inverted orbital polarization in the layers next to $LaAlO_3$, compared to the central part of the YVO_3 layer stack [19].

4.2.1 Orbital polarization profiles in nickelate superlattices

The Ni^{3+} ion in $RNiO_3$ with $R =$ rare-earth ion has nominally a $3d^7$ electron configuration and the octahedral crystal-field of the perovskite structure splits the atomic $3d$ orbital manifold into a lower-lying triply degenerate t_{2g} level that is fully occupied by six electrons, and a higher-lying doubly degenerate e_g level with a single electron. In bulk $RNiO_3$ the two Ni- e_g orbitals with $d_{x^2-y^2}$ and $d_{3z^2-r^2}$ symmetry are equally occupied. Model calculations have shown that the in-plane $d_{x^2-y^2}$ orbital occupation can be stabilized by epitaxial strain and confinement in

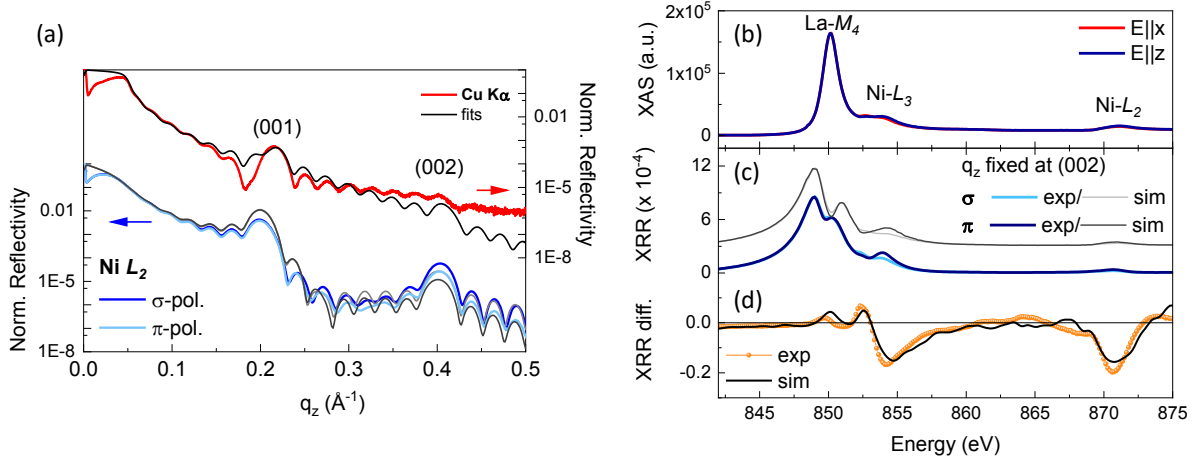


Fig. 13: Experimental data and simulations of XRR data of a $\text{LaNiO}_3\text{-DyScO}_3$ (4/4) superlattice. (a) q_z -dependent reflectivity at fixed energy: non-resonant ($\text{Cu-K}\alpha$) and resonant to Ni-L_2 . (b) Linear dichroism measured in XAS. (c,d) Energy-dependent linear-polarized reflectivity at (002) and the dichroic difference spectrum. Data reproduced from Ref. [50].

a superlattice geometry, resulting in an electronic structure similar to that of the cuprate high-temperature superconductors [52–54]. In order to gain experimental insight on the relative effects of strain and confinement, we have grown superlattices with four-unit-cell-thick layers of metallic LaNiO_3 and layers of different band-insulating RXO_3 ($R = \text{La, Gd, Dy}$ and $X = \text{Al, Ga, Sc}$) by pulsed-laser deposition on substrates that impose either compressive or tensile strain. Using such a symmetric superlattice geometry allows to determine depth-resolved orbital polarization profiles in a quantitative manner by exploiting the depth-dependence of reflectivity at momentum transfer q_z close to the (002) reflection. As introduced in section 3, the XRR analysis relies on optical constants and a structural model. For the analysis we used the software package ReMagX [55]. The structural parameters are obtained by fitting non-resonant, q_z -dependent hard X-ray reflectivity data (Fig. 13(a)), which are then fixed in the following analysis steps. To implement the energy-dependent fine structure across the relevant La-M and Ni-L absorption edges, we used the measured linear polarized XAS (Fig. 13(b)) to build the optical constants of LaNiO_3 in the way shown in Fig. 7.⁴ Then we simulated the reflected intensity measured with fixed q_z as a function of energy (E) (Fig. 13 (c)) and its normalized dichroic difference spectrum (Fig. 13 (d)). To this end, we considered models with different tetragonal scattering tensors (Eq. 8) for f^{IF} in interface layers (B), and f^C in central layers (A) of the LaNiO_3 stacks, keeping the averaged value from XAS fixed. In this way, we were able to determine the redistribution of dichroism between the IF and C layers and the layer-dependent spectra [51]. Then we evaluated them using the sum rule for linear dichroism (Eq. 10), and defined the orbital polarization as

$$P = \left(\frac{4}{n_{eg}} - 1 \right) \frac{X-1}{X+1},$$

⁴For superlattices with the band insulator LaAlO_3 it is important to include the La-M resonances in their optical constants (see Fig. 7), as they are very close to the Ni-L_3 resonance.

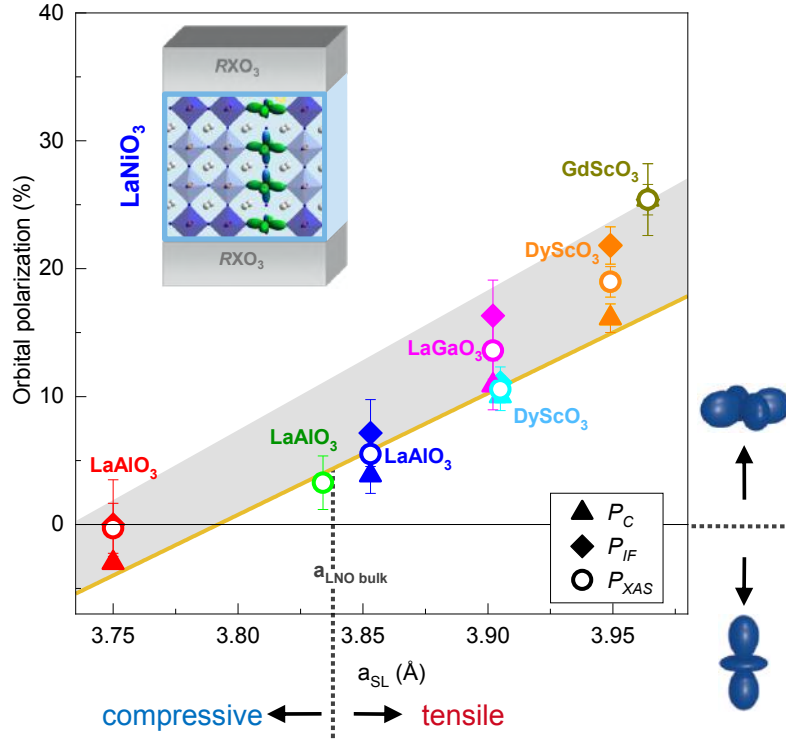


Fig. 14: Layer-resolved orbital polarization, P_C and P_{IF} , as a function of in-plane lattice parameter a_{SL} for LaNiO_3 - RXO_3 superlattices, grown on different strain-inducing substrates and with different composition of the buffer layers as indicated in the labels. The open symbols show the orbital polarization P_{XAS} obtained from the linear dichroism measured in XAS. Data reproduced from Refs. [50, 51].

where $n_{e_g} = 4 - h_{e_g}$ is the sum of e_g electrons. The nickelates are negative charge-transfer insulators with a dominant $3d^8 \underline{L}$ contribution in the ground state [56,49], where \underline{L} denotes an oxygen ligand hole. Therefore the local, atomic Ni- e_g orbitals have rather $n_{e_g} \sim 2$. However, to compare superlattices with possibly different hybridization, i.e., possibly different n_{e_g} , we calculated orbital polarization with $n_{e_g} = 1$ for all different compositions. This means that the orbital polarizations we compare in Fig. 14 can be understood as those of the extended Wannier orbitals, which also have d -orbital symmetry. An illustration of the wave functions, obtained from DFT calculations, and further discussion can be found in Ref. [50]. The layer-resolved orbital polarizations P_C and P_{IF} , together with the layer-averaged values obtained from XAS, P_{XAS} , are shown in Fig. 14 as a function of their in-plane lattice parameters a_{SL} . The lattice parameters have been determined by X-ray diffraction for various (4/4) LaNiO_3 - RXO_3 superlattices grown on substrates with different lattice mismatch. We observed a tendency in all superlattices for the IF layers to have higher orbital polarization than the C layers with values up to 25%, which can be attributed to the confinement effect. However, it can be seen that the strain is the more effective control parameter (yellow line in Fig. 14), while the polarization attributed to the confinement effect from the band insulator layers falls into a comparatively narrow band of $\sim 5\%$ width (grey shaded area in Fig. 14).

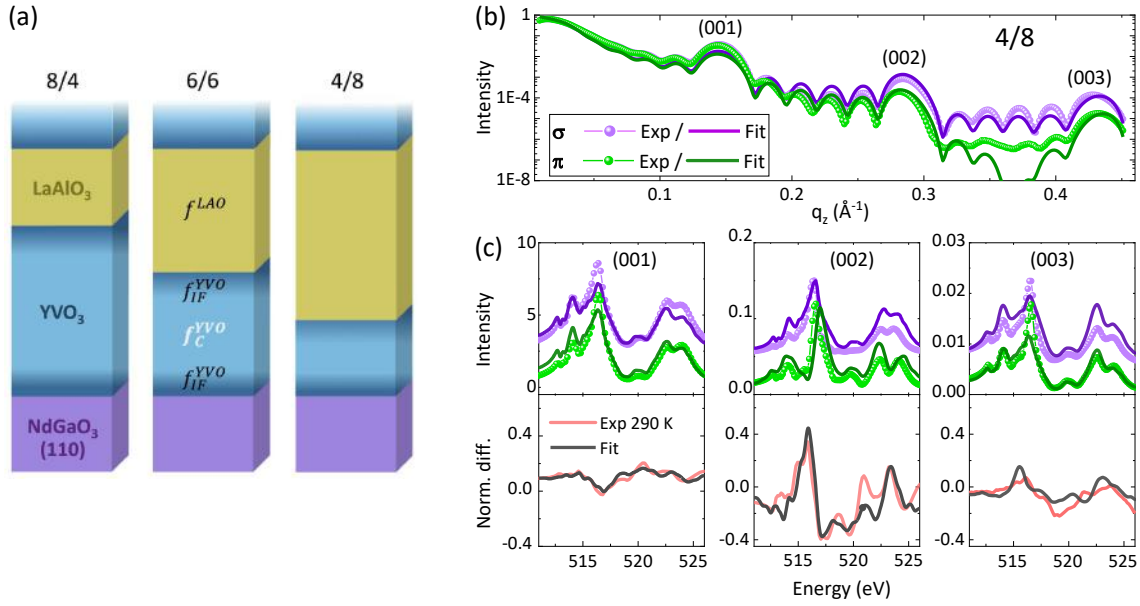


Fig. 15: (a) $\text{YVO}_3\text{-LaAlO}_3$ superlattices with three different stacking sequences, with (8/4), (6/6) and (4/8) consecutive unit cells, were investigated to be as sensitive as possible to orbital reconstructions in interface layers (modelled with scattering factors f^{IF}) and central layers (f^{C}). (b) Representative q_z -dependent and (c) E -dependent scans at momenta fixed to the superlattice reflections $(00l)$ with $l = 1, 2, 3$ for the (4/8) superlattice at room temperature. Reproduced from Ref. [19].

4.2.2 Vanadates - A t_{2g} system

To extend the methodology of orbital reflectometry to a t_{2g} system we have studied $\text{YVO}_3\text{-LaAlO}_3$ superlattices [19]. The compound YVO_3 is a strongly-correlated Mott-Hubbard insulator that shows no metal-insulator transition up to its melting point. The bulk crystallizes in an orthorhombic crystal structure (space group $Pbnm$ with lattice parameters a_o , b_o , and c_o) at room temperature with a V^{3+} electronic configurations shown in the left of Fig. 16(b). The low-temperature properties are governed by different orbital (OO) and spin (SO) ordered phases, which arise from competing crystal-field and superexchange interactions. Below 200 K C -type OO is observed, i.e., there is antiferro-orbital order in the orthorhombic ab_o plane, while along c_o there is ferro-orbital coupling. At 115 K the onset of corresponding G -type SO, and at 77 K a change to G -type OO and C -type SO phase was found [57]. In Ref. [19] we explored possible changes in the orbital occupations in $\text{YVO}_3\text{-LaAlO}_3$ superlattices. While the STEM(-EELS) images shown in Fig. 2 confirmed the high quality of the superlattice structure and the V^{3+} valence state, detailed X-ray diffraction characterization showed that $Pbnm$ -type distortions are also present in the superlattice and that its structure follows the orientation of the substrate, i.e., the orthorhombic c_o axis lies in the interface planes. Accordingly, we rotate the coordinate system for the t_{2g} orbitals for better comparison with the bulk configuration (Fig. 16(b)). To obtain the depth-resolved information, we choose three superlattice structures, with $(\text{YVO}_3)_n/(\text{LaAlO}_3)_m$ bilayers with varying thicknesses of $n = 4, 6, 8$ and $m = 8, 6, 4$

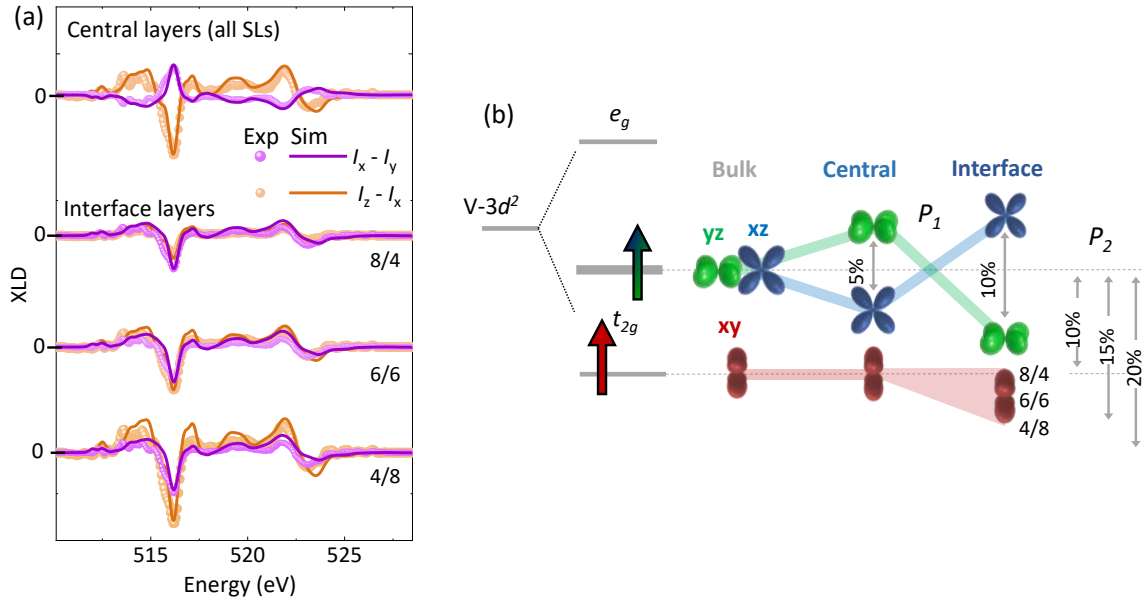


Fig. 16: (a) Experimental (symbols) and fitted (lines) linear dichroism profiles between two polarization pairs for the central (C) layers of all three superlattices (top) and the interfacial (IF) layers of the (8/4), (6/6), and (4/8) superlattices. (b) Schematic representation of the orbital polarization for the bulk, C and IF layers of the superlattices. Taken from [19].

pseudo-cubic unit cells (Fig. 15(a)) to be maximally sensitive to interface reconstructions in the XRR measurements (Fig. 12). We simulated the linear dichroic reflectivity (q_z and E dependent, Fig. 15(b,c)) for different models of the heterostructure, again with f^{IF} and f^C , but now of orthorhombic symmetry, i.e., non-zero $F_{xx} \neq F_{yy} \neq F_{zz}$ in the scattering tensor (5). This is necessary because the t_{2g} , d_{xy} , d_{xz} and d_{yz} orbitals have pairwise lobes in the same spatial directions. In comparison, in the e_g system the $d_{x^2-y^2}$ orbital with z polarization is not accessible. By comparing the results, and then iteratively refining the model we obtained layer-resolved X-ray linear dichroism profiles (Fig. 16(a)) that were then compared with ligand-field cluster calculations to obtain the layer-dependent t_{2g} -orbital polarizations (P_1 and P_2 in Fig. 16(b)). As explained in section 3, the sum rules are not applicable to determine t_{2g} occupations. The results show that d_{xz} and d_{yz} orbital degeneracy is lifted in the superlattices unlike in bulk at room temperature, the d_{xz} - d_{yz} polarization is inverted between the C and IF layers, and the d_{xy} occupation in the IF layers depends on the number of YVO_3 layers (Fig. 16(b)). We also measured the temperature dependence of the spectra shown in Fig. 15(c) and found that the reconstructed orbital occupations are preserved down to 30 K [19].

4.3 Noncollinear magnetic order in nickel oxide heterostructures

As mentioned in the introduction, the accessible Ewald sphere in the soft X-ray region is often limiting for the study of perovskites with comparatively small lattice constants around 4 Å. For example, the ordering vector $q = (1/2 \ 1/2 \ 1/2)$ for the G -type antiferromagnetic order in YVO_3 is not accessible at energies near the V-L edge. The unusual magnetic order observed

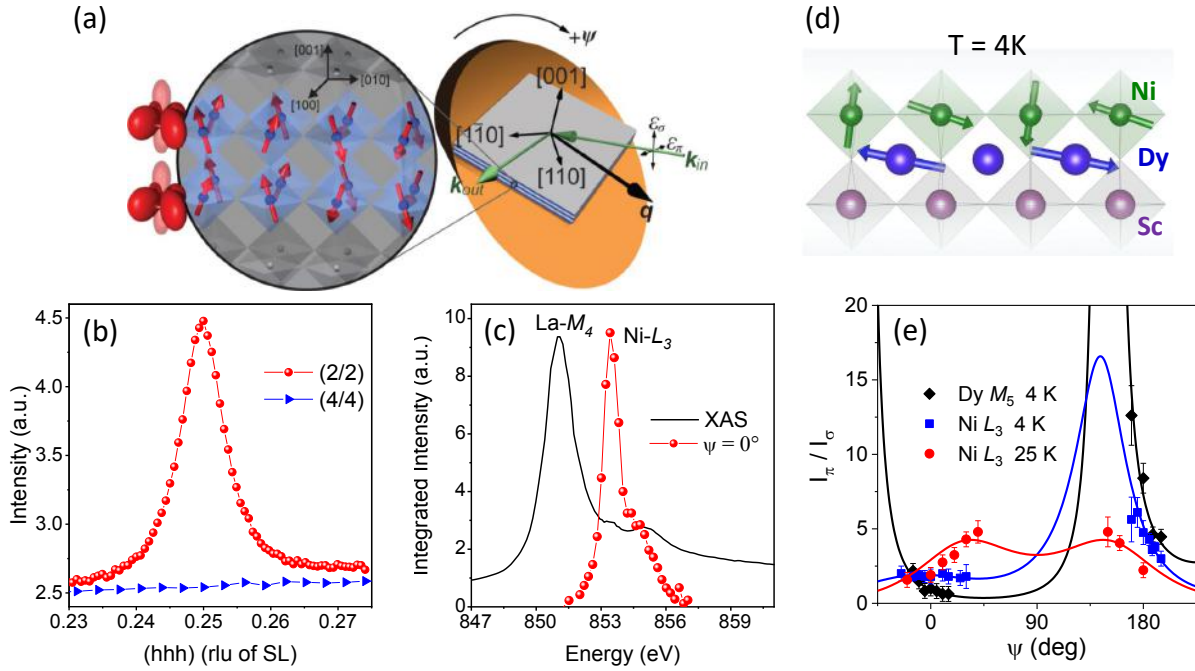


Fig. 17: (a) Sketch of the magnetic order and REXS scattering geometry to study the magnetic order in LaNiO_3 superlattices. The sketch shows the wave vectors of the incoming and outgoing photons (light arrows), the corresponding momentum transfer q , the incoming photon polarization vectors ϵ_σ and ϵ_π , and the azimuthal angle ψ . (b) Scans around q^{mag} at $T = 10$ K and $E = 853.4$ eV for LaNiO_3 - LaAlO_3 superlattices with (2/2) and (4/4) consecutive unit cells. (c) Comparison between XAS and energy dependence of the magnetic Bragg intensity around the Ni- L_3 edge at $\psi = 0^\circ$. (d) Sketch of the Ni-Dy exchange interaction at the interface of a LaNiO_3 - DyScO_3 superlattice derived from the azimuthal dependence (e) of the scattering at q^{mag} , measured resonant to the Dy- M_5 and Ni- L_3 edge at $T = 4$ K. The azimuthal dependence measured at Ni- L_3 at $T = 25$ K corresponds to that of LaNiO_3 - LaAlO_3 (2/2). Figures (a-c) and (d,e) were reproduced from data published in Ref. [58] and Ref. [20], respectively.

in bulk rare-earth nickelates ($R \neq \text{La}$) with an ordering vector $q^{\text{mag}} = (1/4 \ 1/4 \ 1/4)$ in cubic notation is a fortunate exception. It was first studied in NdNiO_3 by REXS at the Ni- L edge in Ref. [59]. We used REXS at the Ni- L edge to study the LaNiO_3 - RXO_3 superlattices that I already introduced in the previous section. LaNiO_3 is the only bulk rare-earth nickelate that is paramagnetic and metallic down to the lowest temperatures [60]. We have shown that when this compound is grown epitaxially between RXO_3 layers in a superlattice, and the thickness is reduced to two unit cells, a magnetic order with q^{mag} is observed [58]. Figure 17(a) shows the scattering geometry used to access the magnetic Bragg peak at energies resonant to the Ni- L_3 edge. While a magnetic Bragg reflection is observed for the (2/2) with two consecutive unit cells each of LaNiO_3 and LaAlO_3 , this is not the case in (4/4) superlattices with thicker layer stacks (Fig. 17(b)). The scattered intensity is strongly enhanced at the Ni- L_3 energy (Fig. 17(c)) and shows an azimuthal dependence (Fig. 17(e)) that is characteristic for a commensurate, non-collinear magnetic order with a ($\uparrow \rightarrow \downarrow \leftarrow \downarrow$)-type order of moments along the cubic perovskite [111] direction (see sketch in Fig. 17(a)). In such an azimuthal scan, the Bragg condition is

preserved and the scattered intensity is measured, while the sample rotates around q_{mag} . During this, the projection of the polarization vectors ϵ_σ and ϵ_π onto the magnetization axis is changed. In the case of the noncollinear order in bulk nickelates, one therefore observes a π -periodic intensity modulation as a function of ψ [59]. For superlattices that are under biaxial strain from the substrate, the direction of the sublattice moments changes due to the changes in d -orbital occupation that controls the magneto-crystalline anisotropy via the spin-orbit coupling [58]. The precise direction of the sublattice magnetization can be determined by simulating the azimuthal dependence (solid lines in Fig. 17(e)). From this and the fact that we observed considerable conductivity in the magnetically ordered state, we conclude that a spin-density wave phase is stabilized in the epitaxial LaNiO_3 superlattice, which has no bulk analogue.

In a second REXS study we examined more closely the (2/2) LaNiO_3 - DyScO_3 superlattice, which, as pointed out above, shows noncollinear q^{mag} order in the Ni spin system below 100 K [20]. Taking advantage of the element sensitivity of REXS by measuring the azimuthal dependence of the scattered intensity at q^{mag} and at energies resonant to Ni- L and Dy- M (Fig. 17(e)), we derived the following scenario. Upon cooling below 18 K, Dy-Ni exchange interactions at the LaNiO_3 - DyScO_3 interfaces lead to a collinear magnetic ordering of the interface Dy moments (note the 2π -periodicity in intensity in the ψ scan) as well as a reorientation of the Ni spins in a direction dictated by the strong magnetocrystalline anisotropy of Dy (Fig. 17(d)). Such exchange interactions between local, paramagnetic rare-earth moments with the magnetic order of transition-metal ions is potentially interesting for manipulating spin structures in devices, as the large Dy moments provide anchoring points to external magnetic fields.

Acknowledgement

This lecture note is largely the result of the author's collaboration with many researchers listed in the references below. My special thanks go to Alex Frano, Meng Wu, Martin Bluschke, Friederike Wrobel and Padma Radhakrishnan, because without their excellent PhD work I would not have been able to show the nice examples in the last section. I would also like to thank Eberhard Goering, who taught me many experimental tricks and proofread these lecture notes.

References

- [1] D.I. Khomskii: *Transition Metal Compounds* (Cambridge University Press, 2014)
- [2] B. Keimer and J.E. Moore, *Nat. Phys.* **13**, 1045 (2017)
- [3] B. Keimer, S.A. Kivelson, M.R. Norman, S. Uchida, and J. Zaanen, *Nature* **518**, 179 (2015)
- [4] H.Y. Hwang, Y. Iwasa, M. Kawasaki, B. Keimer, N. Nagaosa, and Y. Tokura, *Nat. Mater.* **11**, 103 (2012)
- [5] D.N. Basov, R.D. Averitt, and D. Hsieh, *Nat. Mater.* **16**, 1077 (2017)
- [6] D.G. Schlom, L.-Q. Chen, C.-B. Eom, K.M. Rabe, S.K. Streiffer, and J.-M. Triscone, *Annu. Rev. Mater. Res.* **37**, 589 (2007)
- [7] J. Mannhart and D.G. Schlom, *Science* **327**, 1607 (2010)
- [8] H. Takagi and H.Y. Hwang, *Science* **327**, 1601 (2010)
- [9] R. Ramesh and D.G. Schlom, *Nat. Rev. Mater.* **4**, 257 (2019)
- [10] A.M. Glazer, *Acta Crystallogr. A* **31**, 756 (1975)
- [11] J.M. Rondinelli and N.A. Spaldin, *Adv. Mater.* **23**, 3363 (2011)
- [12] M. Bibes and A. Barthelemy, *IEEE Trans. Electron Devices* **54**, 1003 (2007)
- [13] C. Weymann, C. Lichtensteiger, S. Fernandez-Peña, K. Cordero-Edwards, and P. Paruch, *Appl. Surf. Sci.* **516**, 146077 (2020)
- [14] C.B. Eom, R.B. Van Dover, J.M. Phillips, D.J. Werder, J.H. Marshall, C.H. Chen, R.J. Cava, R.M. Fleming, and D.K. Fork, *Appl. Phys. Lett.* **63**, 2570 (1993)
- [15] D.G. Schlom, L.-Q. Chen, X. Pan, A. Schmehl, and M.A. Zurbuchen, *J. Am. Ceram. Soc.* **91**, 2429 (2008)
- [16] B. Jalan, R. Engel-Herbert, N.J. Wright, and S. Stemmer, *J. Vac. Sci. Technol. A* **27**, 461 (2009)
- [17] J. Nordlander, M.A. Anderson, C.M. Brooks, M.E. Holtz, and J.A. Mundy, *Appl. Phys. Rev.* **9** (2022)
- [18] P. Radhakrishnan, B. Geisler, K. Fürsich, D. Putzky, Y. Wang, G. Christiani, G. Logvenov, P. Wochner, P.A. van Aken, R. Pentcheva, and E. Benckiser, *Phys. Rev. B* **105**, 165117 (2022)

- [19] P. Radhakrishnan, B. Geisler, K. Fürsich, D. Putzky, Y. Wang, S.E. Ilse, G. Christiani, G. Logvenov, P. Wochner, P.A. van Aken, E. Goering, R. Pentcheva, and E. Benckiser, *Phys. Rev. B* **104**, L121102 (2021)
- [20] M. Bluschke, A. Frano, E. Schierle, M. Minola, M. Hepting, G. Christiani, G. Logvenov, E. Weschke, E. Benckiser, and B. Keimer, *Phys. Rev. Lett.* **118**, 207203 (2017)
- [21] L.J.P. Ament, M. van Veenendaal, T.P. Devereaux, J.P. Hill, and J. van den Brink, *Rev. Mod. Phys.* **83**, 705 (2011)
- [22] M. Blume in *Resonant Anomalous X-ray Scattering: Theory and Applications*, G. Materlik, J. Sparks, and K. Fischer (eds.) (North-Holland, Amsterdam, 1994)
- [23] J. Fink, E. Schierle, E. Weschke, and J. Geck, *Rep. Prog. Phys.* **76**, 056502 (2013)
- [24] J.P. Hannon, G.T. Trammell, M. Blume, and D. Gibbs, *Phys. Rev. Lett.* **61**, 1245 (1988)
- [25] H. Wadati, A.J. Achkar, D.G. Hawthorn, T.Z. Regier, M.P. Singh, K.D. Truong, P. Fournier, G. Chen, T. Mizokawa, and G.A. Sawatzky, *Appl. Phys. Lett.* **100** 193906 (2012)
- [26] R. Nakajima, J. Stöhr, and Y.U. Idzerda, *Phys. Rev. B* **59**, 6421 (1999)
- [27] K. Zafar, P. Audehm, G. Schütz, E. Goering, M. Pathak, K. Chetry, P. LeClair, and A. Gupta, *J. Electron Spectrosc. Relat. Phenom.* **191**, 1 (2013)
- [28] A. Thompson, D. Attwood, E. Gullikson, M. Howells, K.-J. Kim, J. Kirz, J. Kortright, I. Lindau, P. Pianetta, A. Robinson, J. Scofield, J. Underwood, D. Vaughan, G. Williams, and H. Winick: *X-ray Data Booklet* (Lawrence Berkeley National Laboratory, University of California, 2009)
- [29] M. Haverkort (Ph.D. thesis, University of Cologne, 2005)
- [30] B.T. Thole and G. van der Laan, *Phys. Rev. B* **38**, 3158 (1988)
- [31] M.W. Haverkort, M. Zwierzycki, and O.K. Andersen, *Phys. Rev. B* **85**, 165113 (2012)
- [32] M.D. Núñez Regueiro, M. Altarelli, and C.T. Chen, *Phys. Rev. B* **51**, 629 (1995)
- [33] C.T. Chen, L.H. Tjeng, J. Kwo, H.L. Kao, P. Rudolf, F. Sette, and R.M. Fleming, *Phys. Rev. Lett.* **68**, 2543 (1992)
- [34] C.T. Chen, Y.U. Idzerda, H.-J. Lin, N.V. Smith, G. Meigs, E. Chaban, G.H. Ho, E. Pellegrin, and F. Sette, *Phys. Rev. Lett.* **75**, 152 (1995)
- [35] J. Stöhr, *J. Magn. Mag. Mater.* **200**, 470 (1999)

- [36] D. Alders, L.H. Tjeng, F.C. Voogt, T. Hibma, G.A. Sawatzky, C.T. Chen, J. Vogel, M. Sacchi, and S. Iacobucci, *Phys. Rev. B* **57**, 11623 (1998)
- [37] S. Macke and E. Goering, *J. Phys.: Condens. Matter* **26**, 363201 (2014)
- [38] R.J. Green, R. Sutarto, F. He, M. Hepting, D.G. Hawthorn, and G.A. Sawatzky, *Synchrotron Radiation News* **33**, 20 (2020)
- [39] B. Henke, E. Gullikson, and J. Davis, *Atomic Data and Nuclear Data Tables* **54**, 181 (1993)
- [40] C.T. Chantler, *J. Phys. Chem. Ref. Data* **29**, 597 (2000)
- [41] J. Als-Nielsen and D. McMorrow: *Elements of Modern X-ray Physics*, 2nd Ed. (John Wiley and Sons, Ltd, 2011)
- [42] M. Blume, *J. Appl. Phys.* **57**, 3615 (1985)
- [43] M.W. Haverkort, N. Hollmann, I.P. Krug, and A. Tanaka, *Phys. Rev. B* **82**, 094403 (2010)
- [44] J.M. Tonnerre, M. De Santis, S. Grenier, H.C.N. Tolentino, V. Langlais, E. Bontempi, M. García-Fernández, and U. Staub, *Phys. Rev. Lett.* **100**, 157202 (2008)
- [45] F. Wrobel, B. Geisler, Y. Wang, G. Christiani, G. Logvenov, M. Bluschke, E. Schierle, P.A. van Aken, B. Keimer, R. Pentcheva, and E. Benckiser, *Phys. Rev. Mater.* **2**, 035001 (2018)
- [46] M. Grioni, J.B. Goedkoop, R. Schoorl, F.M.F. de Groot, J.C. Fuggle, F. Schäfers, E.E. Koch, G. Rossi, J.-M. Esteva, and R.C. Karnatak, *Phys. Rev. B* **39**, 1541 (1989)
- [47] J.B. Goodenough, *Phys. Rev.* **100**, 564 (1955)
- [48] J. Kanamori, *J. Phys. Chem. Solids* **10**, 87 (1959)
- [49] G. Sawatzky and R. Green in E. Pavarini, E. Koch, J. van den Brink, G. Sawatzky (eds.): *Quantum Materials: Experiments and Theory*, Modeling and Simulation, Vol. 6 (Schriften des Forschungszentrums Jülich, Germany, 2016)
- [50] M. Wu, E. Benckiser, M.W. Haverkort, A. Frano, Y. Lu, U. Nwankwo, S. Brück, P. Audehm, E. Goering, S. Macke, V. Hinkov, P. Wochner, G. Christiani, S. Heinze, G. Logvenov, H.-U. Habermeier, and B. Keimer, *Phys. Rev. B* **88**, 125124 (2013)
- [51] E. Benckiser, M.W. Haverkort, S. Brück, E. Goering, S. Macke, A. Frañó, X. Yang, O.K. Andersen, G. Cristiani, H.-U. Habermeier, A.V. Boris, I. Zegkinoglou, P. Wochner, H.-J. Kim, V. Hinkov, and B. Keimer, *Nat. Mater.* **10**, 189 (2011)
- [52] J. Chaloupka and G. Khaliullin, *Phys. Rev. Lett.* **100**, 016404 (2008)

-
- [53] P. Hansmann, X. Yang, A. Toschi, G. Khaliullin, O.K. Andersen, and K. Held, Phys. Rev. Lett. **103**, 016401 (2009)
- [54] M.J. Han, C.A. Marianetti, and A.J. Millis, Phys. Rev. B **82**, 134408 (2010)
- [55] S. Macke, A. Radi, J.E. Hamann-Borrero, A. Verna, M. Bluschke, S. Brück, E. Goering, R. Sutarto, F. He, G. Cristiani, M. Wu, E. Benckiser, H.-U. Habermeier, G. Logvenov, N. Gauquelin, G.A. Botton, A.P. Kajdos, S. Stemmer, G.A. Sawatzky, M.W. Haverkort, B. Keimer, and V. Hinkov, Adv. Mater. **26**, 6554 (2014)
- [56] R.J. Green, M.W. Haverkort, and G.A. Sawatzky, Phys. Rev. B **94**, 195127 (2016)
- [57] S. Miyasaka, Y. Okimoto, M. Iwama, and Y. Tokura, Phys. Rev. B **68**, 100406 (2003)
- [58] A. Frano, E. Schierle, M.W. Haverkort, Y. Lu, M. Wu, S. Blanco-Canosa, U. Nwankwo, A.V. Boris, P. Wochner, G. Cristiani, H.U. Habermeier, G. Logvenov, V. Hinkov, E. Benckiser, E. Weschke, and B. Keimer, Phys. Rev. Lett. **111**, 106804 (2013)
- [59] V. Scagnoli, U. Staub, A.M. Mulders, M. Janousch, G.I. Meijer, G. Hammerl, J.M. Tonnerre, and N. Stojic, Phys. Rev. B **73**, 100409 (2006)
- [60] J.B. Torrance, P. Lacorre, A.I. Nazzal, E.J. Ansaldo, and C. Niedermayer, Phys. Rev. B **45**, 8209 (1992)